SACCON Forced Oscillation Tests at DNW-NWB and NASA Langley 14x22-foot Tunnel

Dan D. Vicroy[*]
NASA Langley Research Center, Hampton, VA 23681

Thomas D. Loeser[†]
German-Dutch Wind Tunnels, Braunschweig, Germany

and

Andreas Schütte[‡]
DLR Institute of Aerodynamics and Flow Technology, Braunschweig, Germany

A series of three wind tunnel static and forced oscillation tests were conducted on a generic unmanned combat air vehicle (UCAV) geometry. These tests are part of an international research effort to assess the state-of-the-art of computational fluid dynamics (CFD) methods to predict the static and dynamic stability and control characteristics. The experimental dataset includes not only force and moment time histories but surface pressure and off body particle image velocimetry measurements as well. The extent of the data precludes a full examination within the scope of this paper. This paper provides some examples of the dynamic force and moment data available as well as some of the observed trends.

Nomenclature

A	=	amplitude of oscillation	V	=	velocity
b	=	span	α	=	AoA, angle of attack
C_A	=	axial force coefficient	$\dot{\alpha}$	=	angle of attack rate
C_N	=	normal force coefficient	β	=	sideslip angle
C_Y	=	side-force coefficient	$\dot{\beta}$	=	sideslip angle rate
C_l	=	rolling moment coefficient	ψ	=	yaw angle
C_m	=	pitching moment coefficient	θ	=	pitch angle
C_n	=	yawing moment coefficient	φ	=	roll angle
c_r	=	root chord	ω	=	angular velocity
c_{ref}	=	reference chord	ESP	=	electronically scanned pressure
f	=	oscillation frequency	MRP	=	moment reference point
k	=	reduced frequency	PIV	=	Particle Image Velocimetry
p	=	roll rate	RLE	=	round leading edge
q	=	pitch rate	RLE-FT	=	RLE with fixed transition
r	=	yaw rate	SACCON	=	Stability and Control Configuration
t	=	time	SLE	=	sharp leading edge

---

[*] Senior Research Engineer, Flight Dynamics Branch, MS 308, NASA LaRC, AIAA Associate Fellow.
[†] Project Manager, DNW-NWB, Lilienthalplatz 7, 38108 Braunschweig, Germany.
[‡] Research Engineer, DLR Institute of Aerodynamics and Flow Technology, Lilienthalplatz 7, 38108 Braunschweig, Germany.

I. Introduction

THE role of computational fluid dynamics (CFD) methods in the design process of both air and sea vehicles continues to grow. However, the ability of CFD to accurately predict the static and dynamic stability characteristics of these vehicles has yet to be validated. An Applied Vehicle Technology Task Group (AVT-161) was established by the NATO Research and Technology Organization (RTO) to assess the state-of-the-art in CFD methods for the prediction of static and dynamic stability and control characteristics of military vehicles in the air and sea domains[1,2]. Two highly swept wing configurations were selected for the air vehicle experimental and numerical investigations. The primary configuration was a generic UCAV geometry called SACCON – "**S**tability **A**nd **C**ontrol **CON**figuration". The SACCON model mounted in the Low Speed Wind Tunnel Braunschweig (DNW-NWB) is shown in Fig. 1. The other focus air vehicle of AVT-161 was the X-31[3-5].

This paper presents the results of a series of forced oscillation tests of the SACCON model conducted in both the DNW-NWB low speed wind tunnel and the NASA Langley 14-by 22-Foot Subsonic Tunnel. A complementary set of static data was also collected during these tests and reported in reference 6.
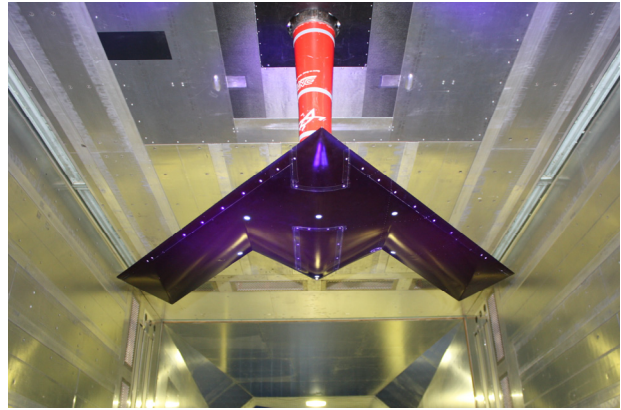
II. Test Setup

A. SACCON Model

The SACCON UCAV has a lambda wing planform with a leading edge sweep angle of 53°, see Figs. 2 and 3. The root chord is approximately 1m and the wing span is 1.53 m. The main sections of the model are the fuselage, the wing section and wing tip. The configuration is defined by three different profiles at the root section of the fuselage, two sections with the same profile at the inner wing, forming the transition from the fuselage to wing and the outer wing section. Finally the

Figure 1. SACCON low speed wind tunnel model on the MPM-"Model Positioning Mechanism" in the closed test section of the Low Speed Wind Tunnel Braunschweig (DNW-NWB).

outer wing section profile has 5° of washout about the leading edge to reduce the aerodynamic loads and shift the onset of flow separation to higher angles of attack.

The leading edge was the only exchangeable part of the model, providing a sharp (SLE) and a variable round leading edge (RLE). The RLE is sharp at the root chord and the leading edge radius is growing in the span-wise direction up to the intersection between fuselage and wing and then decreasing again.
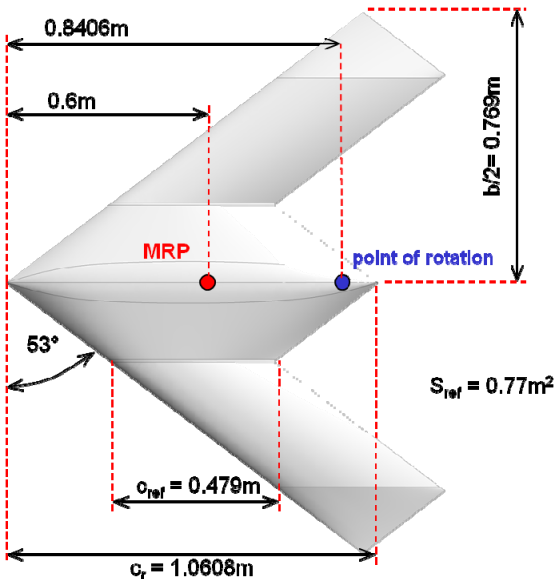
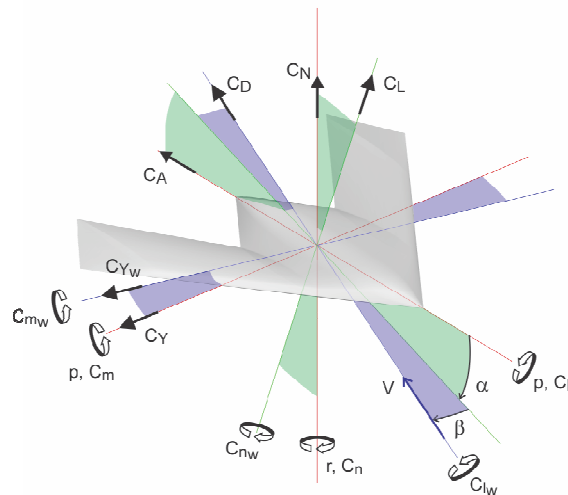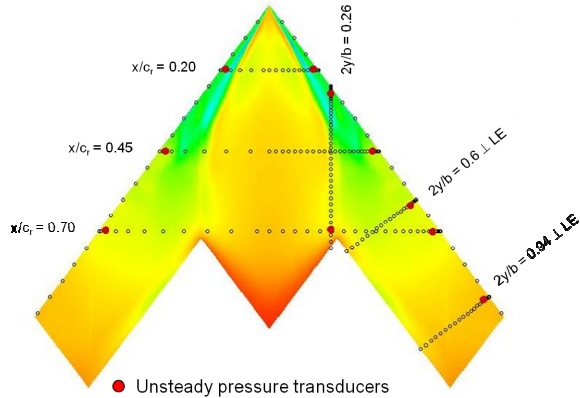**Figure 2. Planform and geometric parameters of the SACCON UCAV configuration.**

Figure 3. SACCON UCAV configuration with force, moment and angle orientations in body and wind axes.
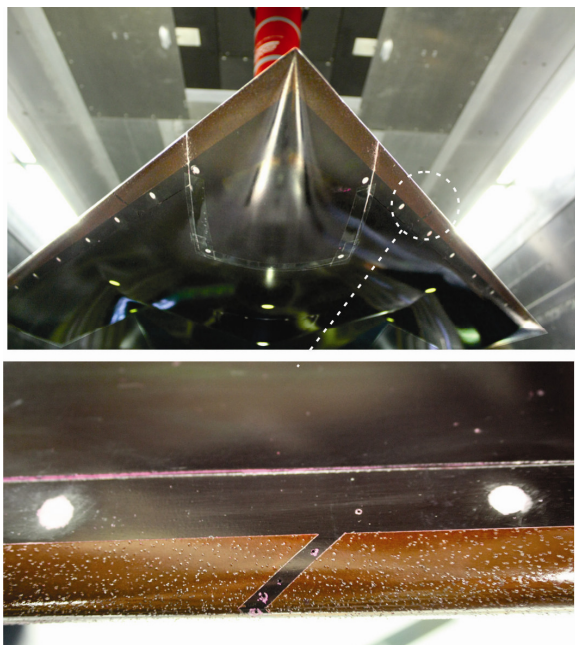
2

Figure 4. Pressure tap location on the upper surface of the SACCON configuration (Surface pressure contour from preliminary CFD calculation).
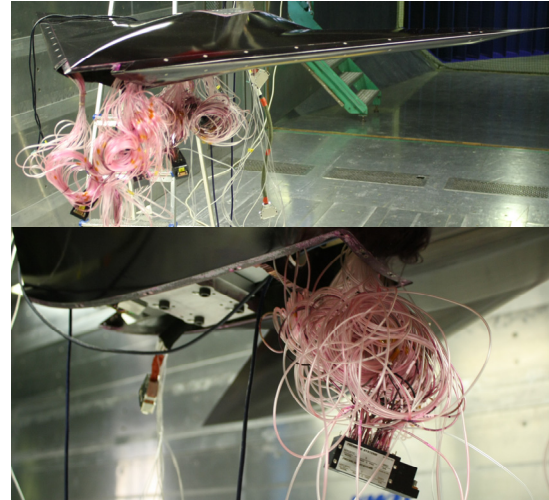
The model is made of carbon fiber reinforced plastic and is very light with an overall weight of less than 10kg (including pressure tubes and ESP modules). The very light design reduces the dynamic inertial loads enabling the use of a smaller, more sensitive balance that provides better force and moment resolution.

The SACCON wind tunnel model is equipped with more than 200 pressure taps on the upper and lower side of the model. The taps are connected with pressure tubes to electronically scanned pressure (ESP) modules within the model. At ten additional positions unsteady pressure transducers are mounted. The location of the pressure taps and transducers are depicted in Fig. 4. The pressure tap locations were selected based on preliminary CFD computations. The aim was to capture the complex vortex flow topology over the configuration at operation points of the trajectory. All pressure tube connections between the pressure taps and ESP modules are of the same length to guarantee the same time dependent behavior for each pressure tap during the unsteady pressure measurements. This leads to big bundles of the flexible tubing which have to be carefully installed to prevent kinks. The tubes bundles which have to be placed inside the model are shown in Fig. 5.

Initial tests with the RLE configuration showed a variable transition line on the upper surface of the model detected by infrared thermography[6]. These measurements led to the decision to prepare the leading edge with a

Figure 5. Pressure tubes and ESP modules of the SACCON wind tunnel model.

carborundum grit trip as it is shown in Fig. 6. The grit was applied to approximately the first 25 mm at the nose to 10mm at the wing tip along both the upper and lower surface. Subsequent infrared thermography showed that after establishing the grit a fully turbulent flow over the upper wing surface could be assumed throughout the oscillation cycle. However, there were no dynamic runs with replicated test conditions with which to compare the effect of the grit on the dynamic forces and moments. All of the round leading edge data presented in this report will be with the carborundum grit. Conversely, all of the sharp leading edge (SLE) data is without grit.

B. Wind Tunnels

The dynamic data for the SACCON model was collected over three wind tunnel test entries in two tunnel facilities. The first two tests were conducted in the DNW-NWB Low-Speed Tunnel located on the DLR site in Braunschweig, Germany, shown in Fig. 7. The last test was conducted in the NASA Langley 14-by-22-Foot Subsonic Tunnel in Hampton, Virginia, USA, show in Fig. 8. Both of these wind tunnels are closed-circuit, atmospheric facilities that can be operated with open or closed test sections. The DNW-NWB test section size is

Figure 6. Leading edge with carborundum grit trip on the RLE-FT configuration (FT: fixed transition).

American Institute of Aeronautics and Astronautics

Figure 7. DNW-NWB low-speed tunnel in Braunschweig, Germany.

Figure 8. NASA Langley 14-by-22-Foot Tunnel in Hampton, Virginia, USA.

3.25 m by 2.8 m (10.6′ by 9.2′). The maximum free stream velocity is V=80 m/s (263 ft/s) with the closed test section and V=70 m/s (230 ft/s) in the open test section. The test section of the Langley 14-by-22-Foot tunnel is 4.42 m by 6.63 m (14.5′ by 21.75′) with a maximum free stream velocity of V=106 m/s (348 ft/s)[8]. Figure 9 provides an illustration of the relative size of the tunnel test sections with the SACCON model in its mounting orientation.
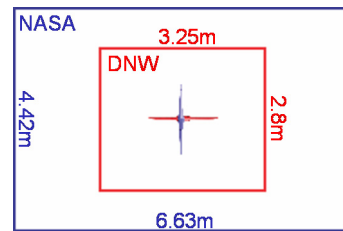
C. Forced Motion Systems

1. MPM system

DNW-NWB's Model Positioning Mechanism (MPM) is a six degree-of-freedom (DOF) parallel kinematics system designed for static as well as for dynamic model support. Characteristic features of this unique test rig are the six constant length struts of ultra high modulus carbon fiber and the six electric linear motors, which move along two parallel rails. The first Eigen frequency at the MRP is above 20 Hz. The MPM is located above the test section and can be operated in the open test section as well as in the closed one. The

Figure 9. Illustration of SACCON model mounting orientation and relative test section size.

location of oscillation axes can be chosen arbitrarily and in addition to classic sinusoidal oscillations the MPM can perform multi-DOF maneuvers. The model location and orientation in the tunnel are determined through an optical photogrammetric system featuring two high speed video cameras. The cameras have been mounted below the test section and acquire 1280x1024 pixel images at 300 frames per second, each. The position and attitude of the model are calculated in real time from the pixel coordinates of three markers, which have been applied to the model surface.

An artist's impression of the MPM carrying the SACCON model is shown in Fig. 10. Although the illustration is depicted with an open test section the SACCON test was conducted in closed configuration. More details concerning the MPM are given in Bergmann et al.[7,9]
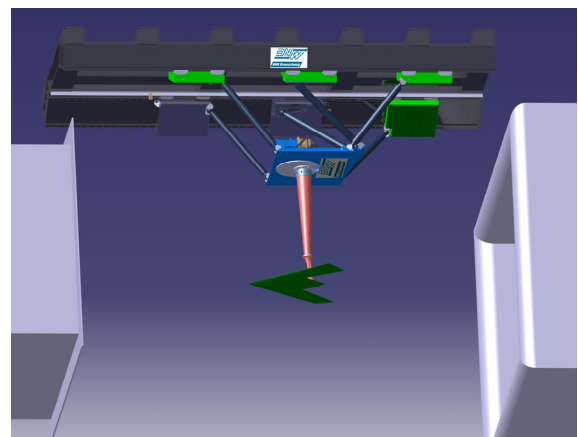
Although the MPM system is capable of complex simultaneous multi-axes motions the SACCON model was only tested with single axis, constant amplitude and frequency, sinusoidal motions. The MPM system was used for pitch and yaw oscillations with ±5° amplitude at frequencies from 1 to 3 Hz. Plunging oscillations were also conducted with ±50mm amplitude at frequencies of 1 and 2.5 Hz.

2. NASA Forced Oscillation Rig

The forced oscillation (FO) test rig in the NASA Langley 14-by-22-Foot Subsonic Tunnel (shown in Fig. 11), can provide constant amplitude and frequency sinusoidal motion in the roll, yaw or pitch axes[10]. The frequency can be set from 0.05 to 1.0Hz at amplitudes up to 30 degrees. The
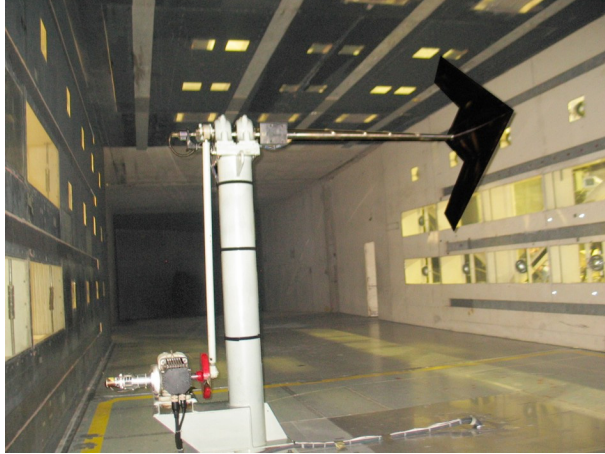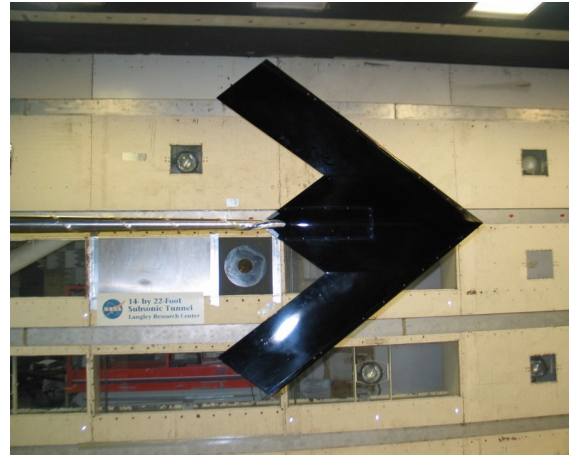

Figure 10. SACCON on the MPM support in the DNW-NWB wind tunnel.

Figure 11. SACCON model mounted on the forced oscillation test rig for yaw oscillations in the NASA Langley 14-by-22-Foot Subsonic Tunnel.

Figure 12. SACCON model with rear sting mount.

model angle of attack is set my rotating the turntable on which the FO rig is mounted. The oscillation angle of the model is measured from an angular position transducer on the FO rig. The NASA rig was used to test the SACCON model in the roll and yaw axes at oscillation amplitudes of ±5°, ±10° and ±15°. Some of the yaw oscillation tests repeated conditions tested in the DNW-NWB Low Speed Tunnel for tunnel to tunnel comparison.

D. Mounting arrangements

The model was designed to accommodate mounting with a rear sting for oscillating in roll, as shown in Fig. 12, or a belly sting for oscillating along the pitch or yaw axis, as shown in Figs. 11 and 13. Different connection links between belly sting support and internal balance at DNW-NWB provide an angle of attack range from -15° to 30°. This is provided by two different rigid cranked yaw links or by using an internal pitch link driven by a 7th axis. The two different basic setups with and without the 7th axis are shown in Fig. 13. The location of the belly sting connection well aft of the moment reference point (MRP) was chosen to minimize the influence of the sting on the overall flow topology. Previous investigations with the X-31 configuration have shown that for the prediction of the total forces and moments the sting support has to be taken into account[11].

It should be noted that since the belly sting attachment and subsequent rotation axis are well aft of the MRP or likely SACCON center of gravity (cg) location the pitch and yaw oscillation data from these tests are not representative of the SACCON dynamic response when rotated about the cg. This data is however valid for the intended purpose of comparing with CFD predictions.

It can be seen in Fig. 13 that the connection between the sting support and internal balance is completely covered by the model fuselage for the configurations with yaw link. These are adapted new designs especially for the SACCON configuration. For the pitch link it was not possible to adapt the design and a cover was used to smooth the geometry in this area.

E. Forces and Moments

An internal six-component strain gauge balance was used for the force and moment measurements. The DNW-NWB wind tunnel test used an Emmen 196-6 balance, whereas the NASA 14x22-foot test used a FF-10D balance. These
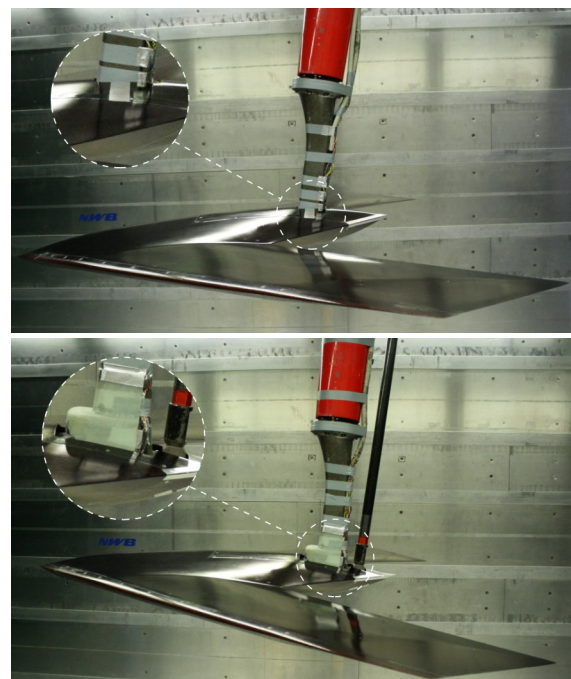
Figure 13. Top: 15° cranked yaw link support. Button: Support with 7th axis and internal pitch link.

5

American Institute of Aeronautics and Astronautics

balances were selected based on comparable load ranges and desired accuracy.

Note that the rolling and yawing moment coefficients were computed using the semi-span rather than span as the reference length. The reference length for the pitching moment coefficient was the reference chord.

F. PIV Measurements

Particle Image Velocimetry (PIV) measurements were performed with two independent systems simultaneously during the second DNW-NWB test by teams from ONERA and DLR. The majority of the PIV measurements were taken statically, however measurements with the model oscillating in pitch were also performed. The PIV cameras were triggered in a phase locked mode with the model oscillation. PIV data were recorded at eight different phase angles over the oscillation cycle. Details of the PIV static and dynamic measurements are provided in references 15 and 16.

G. Test Matrix

The test matrix of model leading edge configurations, mounting arrangements, tunnel conditions and motion parameters for each of the oscillation axes are listed in the appendix in Tables 1 through 4 and illustrated in Figs. 14-16. The motion parameters that were varied were the frequency and amplitude of the sinusoidal oscillation along with the tunnel velocity. The corresponding reduced frequency (k) or Strouhal number and reduced angular rate are shown in the Figs. 14-16 and Tables 1-4. The reduced angular rate is proportional to the tangent of the helix angle of the vehicle rotation relative to the free-stream velocity. For example, the reduced angular rate in roll is proportional to the induced angle of attack at the wing tip due to the rolling motion. The roll angle (φ) during the sinusoidal oscillation is:

$$\varphi(t) = \varphi_0 + A \sin(\omega t) \tag{1}$$

The roll rate is:

$$\dot{\varphi}(t) = p = A\omega \cos(\omega t) \tag{2}$$

The maximum roll rate is:

$$p_{max} = A\omega = 2\pi f A \tag{3}$$

The reduced rotation rate and frequency are non-dimensionalized by the reference length divided by twice the free-stream velocity, with the reference length being the span for roll and yaw and the reference chord for pitch.
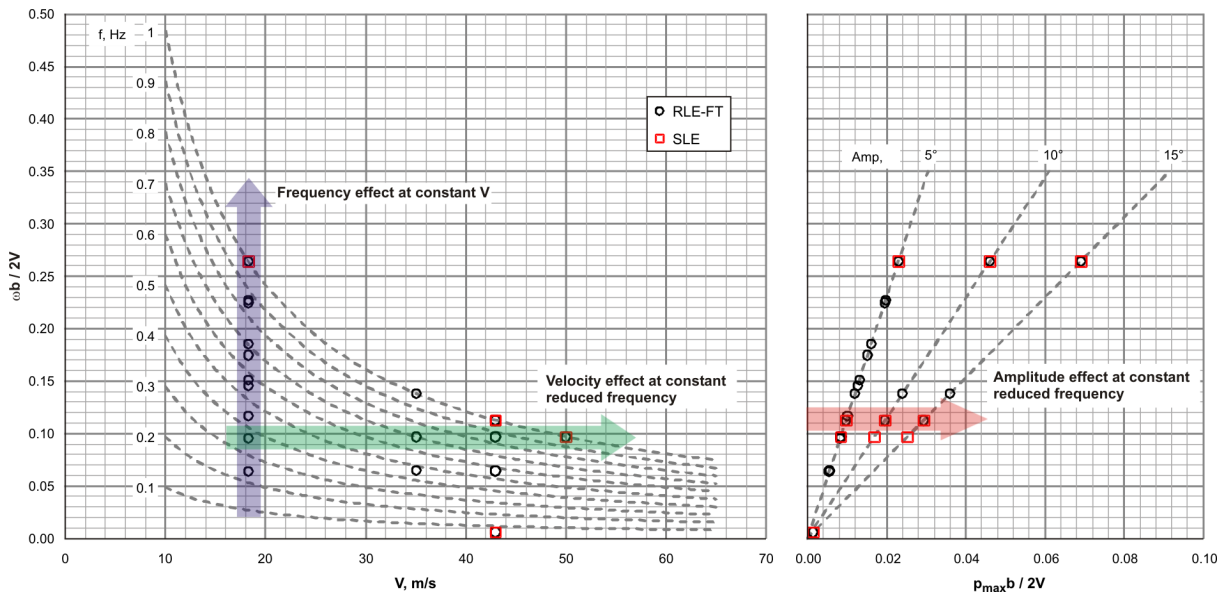

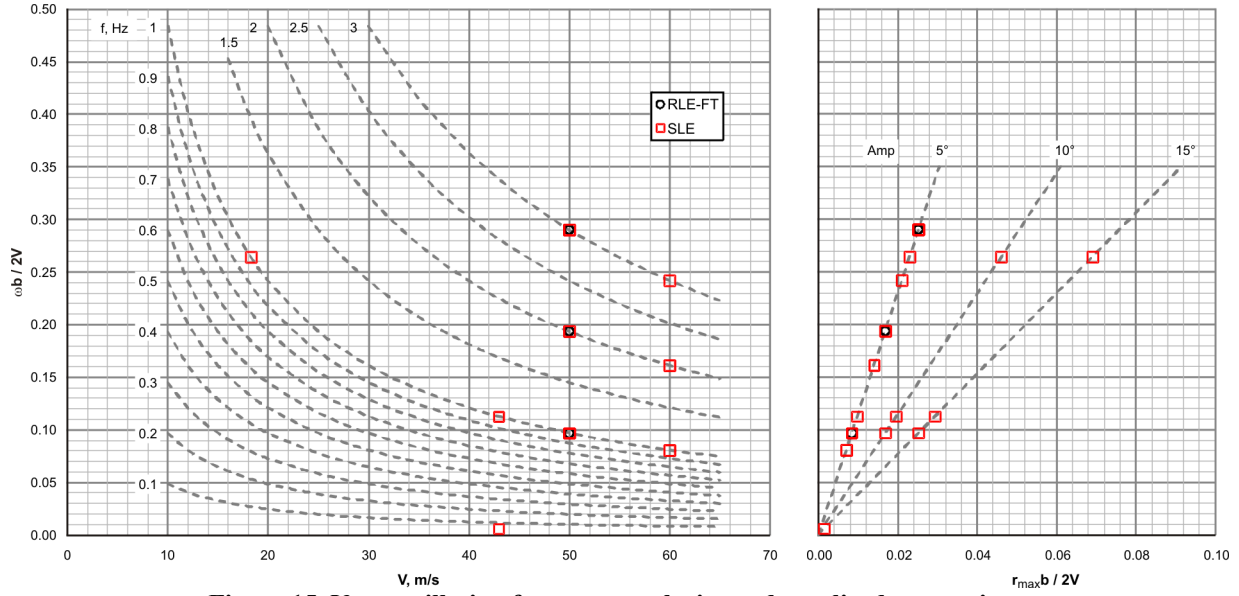**Figure 14. Roll oscillation frequency, velocity and amplitude test points.**

American Institute of Aeronautics and Astronautics

Figure 15. Yaw oscillation frequency, velocity and amplitude test points.

$$\hat{p}_{max} = \frac{p_{max}b}{2V} \tag{4}$$

$$k = \frac{\omega b}{2V} \tag{5}$$

Figure 14 shows that for the roll oscillations the frequency effect was explored with the round leading edge with fixed transition (RLE-FT) configuration at tunnel velocities of 18, 35 and 43 m/s. Similarly, the effect of velocity was tested at reduced frequencies of 0.097 and 0.064. The rate or amplitude effect was also tested at several reduced frequencies with both the RLE-FT and SLE configurations.

Fewer frequency and amplitude combinations were tested in the yaw axis as seen in Fig. 15. Most of the yaw oscillation parameter variations were tested with the SLE configuration.

In the pitch axis (Fig. 16) only a few variations in the oscillation parameter were tested with the majority of the testing with the RLE-FT configuration. Similarly, the plunge oscillations were only conducted at a few test conditions and are not presented graphically.
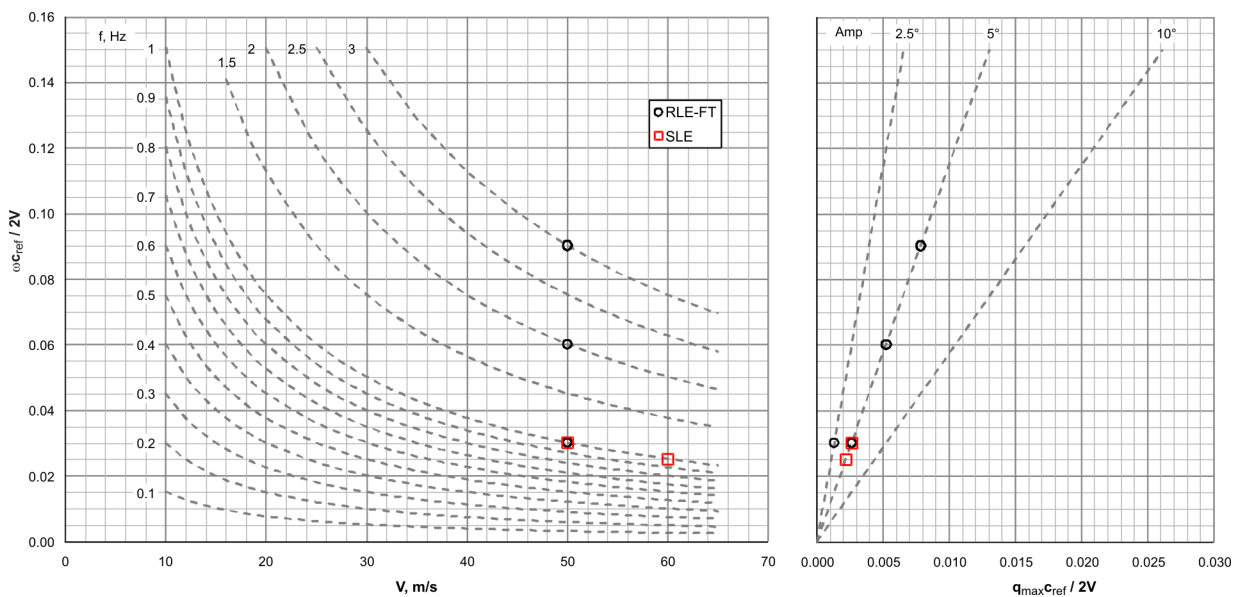

Figure 16. Pitch oscillation frequency, velocity and amplitude test points.

7

American Institute of Aeronautics and Astronautics

All of the pitch and plunge oscillation tests were conducted in the DNW-NWB tunnel. Similarly, all of the roll oscillation tests were done in NASA 14x22-foot tunnel. The only dynamic test conditions replicated in both tunnels were the yaw oscillations at 1Hz and 5° amplitude at AoA's of 10° and 14° with the RLE-FT, and at AoA's of 10° and 15° with the SLE.

III. Data Processing

The force and moment balance signals were sampled at 600 Hz in the DNW-NWB tests and 300 Hz in NASA 14x22-foot test. All balance signals were passed through a low-pass filter with a cut-off frequency of 5 Hz.

There were no corrections for wall or blockage effects applied to the forced oscillation time history data. The DNW-NWB static data is available both with and without wall and blockage corrections. For comparison purposes, all of the data presented in this paper (both static and dynamic) are without wall or blockage corrections. The blockage from the SACCON model at 30° AoA is 4.0% in the DNW-NWB tunnel and 1.3% in the NASA 14x22-foot tunnel.

The NASA static and forced oscillation data were corrected for sting bending. The model attitude in the DNW-NWB tests was measured optically so no sting bending correction was required.

H. Pressure lag corrections

All pressure tube connections between the model pressure taps and ESP modules are of the same length and diameter to assure the same time dependent behavior for each pressure tap during the unsteady pressure measurements. The signals of the ESP modules have been corrected for attenuation and phase shift according to Nyland et al [12]. The ten additional unsteady pressure transducers provide measurements without the pneumatic attenuation and phase shift. However, comparisons of the unsteady pressure transducer measurements with the Nyland corrected pressure tap measurements have not yet been completed.

I. One Cycle Averaging

As was previously noted the dynamic data runs consisted of at least 30 seconds of multi-cycle measured forces, moments, model position and pressures. Each multi-cycle sinusoidal data run was later condensed to a one cycle average loop with standard deviation about fixed oscillation phase angle values. Figure 17 shows an example of a 1Hz pitch oscillation pitching moment data set for the RLE-FT configuration. The nominal AoA is 20° with a pitch amplitude of 5°. Also shown in the figure are the static data and the 1-cycle average with standard deviation bars. The coefficient values at the nominal value crossing points are of particular interest. At these points in the oscillation cycle the rotational acceleration is zero and the rotation rate is the maximum and minimum. Of note is the growth in the standard deviation of the oscillation loop in the higher AoA region of unsteady aerodynamics. An objective of AVT-161 is to assess the ability of current CFD methods to model the physics required to replicate these 1-cycle averaged loops.
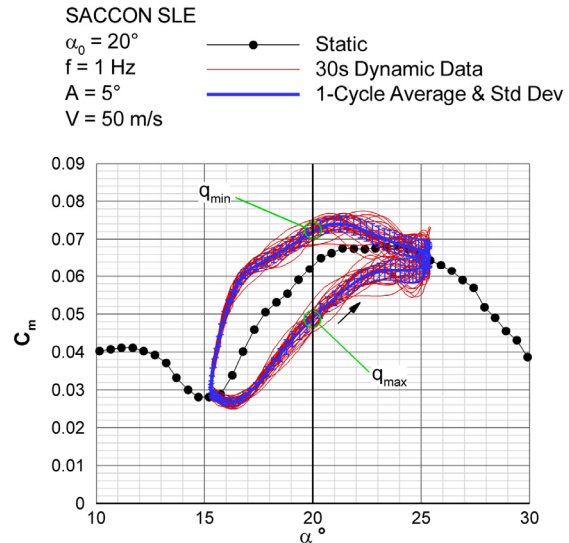
Figure 17. SACCON example of pitch oscillation 1-cycle average pitching moment coefficient verses AoA.

J. Dynamic Derivative Analysis

Beyond the tunnel corrections and 1-cycle averaging some additional data processing was conducted to assess the classic dynamic derivatives from the forced oscillation data. The sinusoidal roll, pitch and yaw oscillations include both body and velocity vector rotation rates. For example, the pitch oscillation motion has both pitch rate (q) and AoA rate ($\dot{\alpha}$). From this type of motion a combined derivative is generally derived, such as:

$$\overline{C_{m_q}} = C_{m_q} + C_{m_{\dot{\alpha}}} \tag{6}$$

The rolling and yawing oscillations produce combined derivates which include sideslip rate terms.

$$\overline{C_{l_p}} = C_{l_p} + C_{l_{\dot{\beta}}} \sin \alpha \tag{7}$$

$$\overline{C_{n_r}} = C_{n_r} - C_{n_{\dot{\beta}}} \cos \alpha \tag{8}$$

To split the combined derivative into the individual terms requires motions with only one of the rotation rates such as plunging which has no pitch rate.

One method of deriving the combined dynamic derivatives from the oscillation data, often referred to as the "single point" method, is to compute the difference of the maximum and minimum rate coefficient values divided by the difference in the maximum and minimum rates[13,14]. For example:

$$\overline{C_{m_q}} = \frac{C_{m_{(q_{max})}} - C_{m_{(q_{min})}}}{\frac{\bar{c}}{2V}(q_{max} - q_{min})} \tag{9}$$

Some examples of the combined dynamic derivatives computed in this manner are presented the following section.

IV. Results and Discussion

The breadth of dynamic data collected during the three wind tunnel test entries exceeds what can be fully examined within the scope of this paper. This paper will highlight the observed trends and provide selected examples for each of the oscillation axes. The number and size of the remaining data figures prohibits them from neatly merging with the text and are presented in the appendix.

K. Roll oscillation data

All of the roll oscillation data were collected during the NASA 14x22-foot Tunnel test with an aft sting mount, as previously shown in Fig. 12. An example of the roll oscillation dynamic effects on the 1-cycle averaged lateral-directional force and moment coefficients are shown in Fig. 18 for RLE-FT configuration at AoA values from 0° to 20° in 5° increments. Up through 10° AoA the 1-cycle averaged loops are very elliptical with minimal deviation. Above 10° the loops are more irregular and asymmetric with increasing standard deviation. As previously noted in Fig. 17, this deviation increase is indicative of increased unsteady flow behavior at higher AoA. The lateral asymmetry and the vertical offset of the ellipse centroid are indicative of small asymmetries in the model geometry and potential flow angularity. These geometric asymmetries will not likely be included in the CFD predictions for which this data is being generated. To facilitate comparisons of the roll and yaw oscillation dynamic data with the CFD predictions the vertical offsets at zero roll or yaw angle axis are subtracted from the dynamic data and the data is presented as the change (Δ) in the forces and moments, as shown in Fig. 19. The vertical offset is computed as the average of the two zero axis crossing values.

Figure 20 shows the roll oscillation coefficient loops for the SLE configuration at the same AoA increments, frequency, velocity and amplitude as the RLE-FT data shown in Fig. 19. The rolling moment coefficient loops for both leading edge configurations show similar trends with AoA. They are all elliptical and counterclockwise with the 20° AoA loop having a significant change in slope. The elliptical shape of the coefficient loop is significant in that it is easily modeled with the classic linear flight mechanics coefficient model.

$$C_l = \frac{l}{\bar{q}\,S\,b/2} = C_{l_\beta}\beta + C_{l_{\dot{\beta}}}\frac{\dot{\beta}b}{2V} + C_{l_p}\frac{pb}{2V} + C_{l_r}\frac{rb}{2V} \tag{10}$$

The slope of the ellipse major axis is proportional to the C_{l_β} term and the direction of the oscillation loop indicates the sign of the damping derivative C_{l_p}. Clockwise oscillation loops represent positive derivatives (propelling), counter-clockwise loops are negative (damping).

The yawing and side-force coefficient loops are more irregular and asymmetric and show the biggest difference between the leading edge configurations, particularly at 15° AoA. In this AoA region there is significant change in the forces and moments for both leading edge configurations. This will be more apparent in the pitch oscillation data presented in the next section. Most of the remaining examples will be from this 14° to 15° AoA region.

The velocity effect was explored with the RLE-FT configuration at four velocities with the same reduced frequency, as previously illustrated in Fig. 14. Figure 21 shows the lateral-directional coefficient loops at 14° AoA. The lower velocities showed greater lateral asymmetry and standard deviation. At the higher velocities the loops were more elliptical and consistent. Note however that the zero axis crossing values are nearly constant for all velocities.

The effect of frequency at a fixed velocity is shown in Fig. 22. The higher frequency increases the vertical thickness of the coefficient loops but maintains the general shape. The rolling moment loops remain elliptical whereas the yawing moment and side-force loops are asymmetric.

The effect of oscillation amplitude at a fixed reduced frequency is shown in Fig. 23. The increased oscillation amplitude tends to magnify the rolling moment loops. The yawing and side-force show not only an increase in the size of the loops but a magnification of the asymmetry as well with the oscillation loop overlapping. The loop overlapping is indicative of a sign reversal in the damping characteristics which may be due to flow separation at the increased rotation rates of the higher amplitudes.

The effect of all the motion variables (frequency, amplitude and velocity) on the roll axis dynamic derivatives is illustrated in Fig. 24 which shows the coefficient values at the zero roll angle axis crossing (peak rate, zero acceleration) with their corresponding peak reduced rate values. The crossing pair values shown in the figure are for all the frequency and amplitudes tested at the given velocity. Recall from the *Dynamic Derivative Analysis* section that the dynamic derivative is the slope of the line through the crossing pair values. The figure shows the roll damping derivative to be negative and invariant over a wide amplitude, frequency and velocity range. The side-force and yawing moment show a slight shift in slope or derivative value with velocity and at large reduced rates.

Figure 25 shows all the combined roll derivative values for both leading edge configurations. The dynamic derivatives for both leading edge configurations are roughly the same up through 10° AoA. Above 10° there is considerable variation in the derivative values. These large variations highlight the limits of this simple linear model to capture the non-linear character of the forces and moments at these higher angles.

L. Pitch oscillation data

All of the pitch oscillation data were collected in the DNW-NWB low-speed tunnel as listed in Table 1. The pitch dynamic effects on the longitudinal forces and moments of the SACCON RLE-FT configuration are shown in Figs. 26 and 27 for 1 and 3Hz oscillation frequencies, respectively. The 5° amplitude oscillations are shown about nominal angle of attacks of 5°, 10°, 15° and 20°. The dynamic damping effect is seen as the difference between the static and dynamic measurements. The offset between the axial force static and dynamic data is currently unexplained and under review. The dynamic data should encompass the static data. The pitching moment showed a larger dynamic effect than either the normal or axial force coefficients. Both force coefficients showed very little dynamic effect below 15° AoA. In the higher AoA range near flow separation the lower frequency (1 Hz) resulted in a more non-linear behavior than the higher 3 Hz data. This is presumed to be due to the flow dynamics having sufficient time to transition between states at the lower frequencies. At the higher frequencies the flow does not have time to transition resulting in a more linear behavior. The greater CFD challenge is in capturing the lower frequency non-linear dynamic effect.

The effect of the SLE on the pitch dynamics is shown in Fig. 28 for the 1Hz pitch oscillation runs. The dynamic effects are similar to the RLE-FT results shown in Fig. 27. The SLE axial data did not have the large offset between the static and dynamic data seen with the RLE-FT configuration. The static data of both leading edge configurations show a large pitch and axial force change near 15° AoA.

The dynamic testing in pitch axis did not cover as large a variation in test conditions as the roll and yaw axes, as previously illustrated in Figs. 14-16. The effect of frequency was just reviewed and the effects of velocity and amplitude were not explored.

Figure 29 shows the pitch axis combined dynamic derivatives for all the conditions tested. As with the roll axis the leading edge configuration did not show a significant difference in the dynamic derivative values except at the higher AoA where there is large dispersion in the values. The normal and axial force derivatives have very small

values up through 10° AoA with a large change in value above 15°. This characteristic was also noted in the 1-cycle average loops presented in Figs. 26-28. The pitching moment however showed some damping value even at the lowest AoA values.

M. Plunging data

A relatively small set of plunging data was collected compared to the rotational oscillation testing as evidenced in the test matrix Tables 1-4. The plunging amplitude was 0.05 meters and the free-stream velocity was 50 m/s. This resulted in an AoA change of ±0.36° and ±0.90° for the 1.0 Hz and 2.5 Hz oscillation frequencies, respectively. An example of the resultant longitudinal force and moment loops is shown in Fig. 30 for the 2.5 Hz plunging of the SLE configuration.

The longitudinal AoA rate derivatives from the plunging data are shown in Fig. 31. There is not must difference between the leading edge configurations and considerable scatter in the derivative values at 20° AoA.

N. Yaw oscillation data

An example of the yaw oscillation effects on the lateral-directional force and moment coefficients about a 15° nominal AoA are shown in Fig. 32 for the SLE configuration at three oscillation frequencies. The lack of any vertical surfaces on the SACCON configuration results in fairly small yaw oscillation effects. As with the roll oscillation data there are lateral asymmetries of the data indicative of small asymmetries in the model geometry and potential flow angularity. The increased frequency increased the vertical thickness of the force and moment loops similar the roll and pitch data.

The yaw oscillation data for the RLE-FT configuration about a 14° nominal AoA at the same test conditions are shown in Fig. 33. In this AoA region the leading edge appears to have a significant effect on the shape of the yaw oscillation force and moment loops. The RLE-FT rolling and yawing moment data show very little dynamic effect in terms of the vertical thickness of the loops and are in the opposite direction from the SLE data. The resulting dynamic derivatives will be small negative (damping) values.

An example of the yaw amplitude effect is shown in Fig. 34 for the SLE configuration at a fixed velocity and frequency. These data are from the NASA test and show a similar loop magnification effect as seen with the roll amplitude in Fig. 23. The lower amplitude data was more asymmetric that the higher amplitude data which also has higher angular rates. The higher rates may be preventing the flow from transitioning between separation and attachment states. Future examination of the pressure time history data may reveal the dynamic flow mechanics.

The only dynamic test conditions replicated in both tunnels were the yaw oscillations at 1 Hz and 5° amplitude with the SLE configuration at AoA's of 10° and 15°, and with the RLE-FT configuration at AoA's of 10° and 14°. The tunnel to tunnel comparisons for the SLE and RLE-FT configurations are shown in Figs. 35 and 36, respectively. There is generally good agreement in the loop shapes with the largest difference occurring at the amplitude peaks. The zero yaw angle axis crossing values are nearly the same which will yield similar dynamic derivatives. The repeatability of the DNW-NWB data is very good with each run 1-cycle average loop overlaying the other.

Figure 37 shows the yaw axis combined dynamic derivatives for all the conditions tested. As with the previous axes the leading edge configuration did not show a significant difference in the dynamic derivative values. The derivative values were nearly zero up through 10°. As noted in the discussion of Figs. 32 and 33 the SLE had larger derivative magnitudes at 15° AoA than the RLE-FT at 14°, which were still near zero.

V. Summary

The three wind tunnel tests of the SACCON model in the DNW-NWB low-speed tunnel and the NASA Langley 14-by-22-Foot Subsonic tunnel have provided a wealth of static and dynamic data for CFD validation. This dataset includes not only force and moment time histories but surface pressure and off body particle image velocimetry (PIV) measurements as well. The extent of the data precludes a full examination within the scope of this paper. This paper has provided some examples of the dynamic force and moment data available as well as some of the observed trends.

The most interesting and challenging dynamics for CFD to replicate occur in the AoA range between 10° and 20° for the SACCON. Below 10° AoA the statics and dynamics are very linear with little or no dynamic hysteresis. The only significant dynamic derivative values in this low AoA range are seen in the roll axis data and the pitching moment data in the pitch axis. These trends are as expected for a flying wing configuration. The lack of vertical surfaces resulted in very little yaw effect in the low AoA range.

The repeatability of the DNW-NWB dynamic data was very good. The limited tunnel to tunnel comparison data also showed good agreement in the yaw oscillation loop shapes with the largest difference occurring at the peak yaw deflection angles.

VI.   Recommendations

The extent of the data collected during the three test of the SACCON model has created a created a considerable data analysis challenge. This paper has highlighted some of the force and moment analysis but significant work remains to correlate this data with the dynamic surface pressure and PIV measurements. Such analysis will provide a better understanding of the dynamic flow topology for correlation with CFD predictions.

In an effort to minimize the aerodynamic effect of the belly mount, the attachment point and resultant rotation axes for the pitch and yaw oscillation were well aft of the moment reference point or likely center of gravity location for the SACCON configuration. Consequently, the pitch and yaw oscillation data from these tests are not representative of the SACCON dynamic response when rotated about the center of gravity and should not be used as such.. This data is however valid for the intended purpose of comparing with CFD predictions.

VII.   Conclusion

A significant low-speed dataset of the SACCON model has been collected for the purpose of CFD validation. The AoA region between 10° and 20° provides the most challenging dynamic flow topology to replicate. If CFD can replicate the 1-cycle averaged dynamic hysteresis loops in this AoA region then the relevant flow physics have been captured.

Acknowledgments

References

[1]Schütte, A.; Cummings, R.; Loeser, T.; and Vicroy, D.: "Integrated Computational/Experimental Approach to UCAV and Delta-Canard Configurations Regarding Stability & Control," *4th Symposium on Integrating CFD and Experiments in Aerodynamics*, Von Karman Institute, Rhode-Saint-Genèse, Belgium, September 14-16, 2009.

[2]Cummings, R.; and Schütte, A.: "Computational/Experimental Approach to UCAV Stability & Control Estimation: Overview of NATO RTO AVT-161," AIAA-2010-4392, *28th AIAA Applied Aerodynamics Conference*, Chicago, IL, June 28 – July 1, 2010.

[3]Schütte, A.; Loeser, T.; and Oehlke, M.: "Prediction of the Flow Around the X-31 Aircraft Using Two Different CFD Methods," AIAA-2010-4692, *28th AIAA Applied Aerodynamics Conference*, Chicago, IL, June 28 – July 1, 2010.

[4]Jirasek, A.; and Cummings, R.: "Reduced Order Modeling of X-31 Wind Tunnel Model Aerodynamic Loads," AIAA-2010-4693, *28th AIAA Applied Aerodynamics Conference*, Chicago, IL, June 28 – July 1, 2010.

[5]Tomac, M.; and Rizzi, A.: "Comparing & Benchmarking Engineering Methods on the Prediction of X-31 Flying Qualities," AIAA-2010-4694, *28th AIAA Applied Aerodynamics Conference*, Chicago, IL, June 28 – July 1, 2010.

[6]Loeser, T.; Vicroy, D.; and Schütte, A.: "SACCON Static Wind Tunnel Tests at DNW-NWB and 14'x22' NASA LaRC," AIAA-2010-4393, *28th AIAA Applied Aerodynamics Conference*, Chicago, IL, June 28 – July 1, 2010.

[7]Bergmann, A.; Hübner, A.-R.: "Integrated Experimental and Numerical Research on the Aerodynamics of Unsteady Aircraft," *3rd International Symposium on Integrating CFD and Experiments in Aerodynamics*, ASAFA, Colorado, June 20-21, 2007.

[8]Gentry, Jr., G.;Quinto, P. F.; Gatlin, G. M.; Applin, Z. T.: "The Langley 14- by 220Foot Subsonic Tunnel: Description, Flow Characteristics, and Guide for Users," NASA TP-3008, September, 1990.

[9]Bergmann, A.; Hübner, A.-R.; Loeser, T.: "Experimental and numerical research on the aerodynamics of unsteady moving aircraft," *Progress in Aerospace Sciences*, Volume 44, Issue 2, February 2008, Pages 121-137.

[10]Owens, D. B.; Brandon, J. M.; Fremaux, C. M.; Heim, E. H.; Vicroy, D. D.: "Overview of Dynamic Test Techniques for Flight Dynamic Research at NASA LaRC," AIAA -2006-3146, *25th AIAA Aerodynamic Measurement Technology and Ground Testing Conference*, San Francisco, California, June 5-8, 2006.

[11]Schütte, A.; Rein, M.; Höhler, G.: "Experimental and numerical aspects of simulating unsteady flows around the X-31 configuration," *3rd International Symposium on Integrating CFD and Experiments in Aerodynamics*, ASAFA, Colorado, June 20-21, 2007. Proc. IMechE, Part G: *J. Aerospace Engineering*, 2009, 223(G4) 309-321. DOI: 10.1243/09544100JAERO387.

[12]Nyland, T.W.; Englund, D.R.; Anderson, R.C.: "On The Dynamics of Short Pressure Probes: Some Design Factors Affecting Frequency Response*,"* NASA TN D-6151 (1971).

[13]Brandon, J. M.; Foster, J. V.: "Recent Dynamic Measurements and Considerations for Aerodynamic Modeling of Fighter Airplane Configurations," AIAA 98-4447, August 10-12, 1998.

[14]Brandon, J. M.; Foster, J. V.; Gato, W.; and Wilborn, J. E.: "Comparison of Rolling Moment Characteristics During Roll Oscillations for a Low and a High Aspect Ratio Configuration," AIAA 2004-5273, *AIAA Atmospheric Flight Mechanics Conference and Exhibit*, Providence, RI, August 16-19, 2004.

[15]Gilliot, A.: "Static and Dynamic SACCON PIV Tests – Part I: Forward Flow Field," AIAA-2010-4395, *28th AIAA Applied Aerodynamics Conference*, Chicago, IL, June 28 – July 1, 2010.

[16]Konrath, R.; Roosenboom, E.; Schröder, A.; Pallek, D.; and Otter, D.: "Static and Dynamic SACCON PIV Tests – Part II: Aft Flow Field," AIAA-2010-4396, *28th AIAA Applied Aerodynamics Conference*, Chicago, IL, June 28 – July 1, 2010.

Appendix

Table 1 - Pitch oscillation test matrix

Tunnel	Test	Run	Config.	α deg	Amp deg	f Hz	V m/s	$\frac{\omega c}{2V}$	q_{max} °/s	$\frac{q_{max}c}{2V}$	Duration sec	Mount
DNW-NWB	2373	1003-1012	RLE	0				0.025		0.0022		0° Yaw link
		1013-1022		5			60					
		1023-1032		10								
	2426	1604-1613		10	5				31.4			15° Yaw link
		1614-1623				1				0.0026		
		1084-1088		15				0.030				
		1104-1108										
		1079-1083		16.5	2.5				15.7	0.0013		
		1094-1103										
	2373	1630-1639	RLE-FT	5					31.4	0.0026	30	6° pitch link
		1640-1649				3	50	0.090	94.2	0.0079		
		1650-1659		10		1		0.030	31.4	0.0026		
		1660-1669				3		0.090	94.2	0.0079		
		1670-1679		15		1		0.030	31.4	0.0026		
		1715-1724				2		0.060	62.8	0.0053		
		1680-1689			5	3		0.090	94.2	0.0079		
		1690-1699		20		1		0.030	31.4	0.0026		
		1725-1734				2		0.060	62.8	0.0053		
		1700-1709				3		0.090	94.2	0.0079		
		1099-1108	SLE	5			60	0.025		0.0022		0° Yaw link
		1109-1118		10					31.4			
		1194-1203		15		1						
		1204-1213		20			50	0.030		0.0026		15° Yaw link
		1214-1223		25								

Table 2 - Plunging oscillation test matrix

Tunnel	Test	Run	Config.	α deg	Amp m	f Hz	V m/s	$\frac{\omega c}{2V}$	$\Delta\alpha$ deg	$adot_{max}$ °/s	Duration sec	Mount
DNW-NWB	2373	1544-1553	RLE-FT	10								15° Yaw link
		1554-1563		15		1		0.030	0.36	2.26		
		1564-1573		20								
		1574-1583		10								
		1584-1593		15		2.5		0.075	0.90	14.14		
		1594-1603		20	0.05		50				30	
		1264-1273	SLE	10								
		1224-1233		15		1		0.030	0.36	2.26		
		1244-1253		20								
		1274-1283		10								
		1234-1243		15		2.5		0.075	0.90	14.14		
		1254-1263		20								

American Institute of Aeronautics and Astronautics

Table 3 - Roll oscillation test matrix

Tunnel	Test	Run	Config.	α deg	Amp deg	f Hz	V m/s	$\frac{\omega b}{2V}$	p_{max} °/s	$\frac{p_{max}b}{2V}$	Duration sec	Mount
NASA 14x22	134	17	RLE-FT	5 10 14 15 20	5	0.24	18	0.063	7.5	0.0055	179	Aft sting
		18		5 10 14 15 20	5	0.36	18	0.095	11.3	0.0083	119	
		19		5 10 14 15 20	5	0.44	18	0.116	13.8	0.0101	97	
		20		10 14 15 20	5	0.55	18	0.145	17.3	0.0127	78	
		21		10 14 15 20	5	0.57	18	0.151	17.9	0.0131	75	
		22		10 14 15 20	5	0.66	18	0.174	20.7	0.0152	65	
		23		10 14 15 20	5	0.70	18	0.185	22.0	0.0161	61	
		24		10 14 15 20	5	0.85	18	0.225	26.7	0.0196	50	
		25		10 14 15 20	5	0.86	18	0.227	27.0	0.0198	50	
		12		0 5 10 14 15 20		1.00	18	0.264	31.4	0.0231	43	
		31		5 10 14 15 20	10	1.00	18	0.264	62.8	0.0461	43	
		35		0 5 10 14 15 20	15	1.00	18	0.264	94.2	0.0692	43	
		28		5 10 14 15 20	5	0.47	35	0.065	14.8	0.0057	91	
		26		5 10 14 15 20	5	0.70	35	0.096	22.0	0.0084	61	
		13		0 5 10 14 15 20		1.00	35	0.138	31.4	0.0120	43	
		32		5 10 14 15 20	10	1.00	35	0.138	62.8	0.0241	43	
		36		5 10 14 15 20	15	1.00	35	0.138	94.2	0.0361	43	
		29		5 10 14 15 20	5	0.57	43	0.064	17.9	0.0056	75	
		30		5 10 14 15 20	5	0.86	43	0.097	27.0	0.0084	50	
		15		0 5 10 14 15 20		1.00	43	0.112	31.4	0.0098	43	
		33		0 5 10 14 15 20	10	1.00	43	0.112	62.8	0.0196	43	
		38		0 5 10 14 15 20	15	0.05	43	0.006	4.7	0.0015	100	
		37		0 5 10 14 15 20	15		43	0.112	94.2	0.0294		
		16	SLE	0 5 10 14 15	5	1.00	50	0.097	31.4	0.0084	43	
		49		0 5 10 15 20 25	5	1.00	18	0.264	31.4	0.0231	43	
		46		5 10 15 20 25	10	1.00	18	0.264	62.8	0.0461	43	
		43		5 10 15 20 25	15	1.00	18	0.264	94.2	0.0692	43	
		50		0 5 10 15 20 25	5		43	0.112	31.4	0.0098	43	
		47		0 5 10 15 20 25	10		43	0.112	62.8	0.0196	43	
		42		0 5 10 15 20 25	15	0.05	43	0.006	4.7	0.0015	100	
		44		5 10 15 20 25	15		43	0.112	94.2	0.0294		
		51		0 5 10 15	5	1.00	50	0.097	31.4	0.0084	43	
		48		0 5 10 15	10	1.00	50	0.097	62.8	0.0169	43	
		45		0 5 10 15	15	1.00	50	0.097	94.2	0.0253	43	

American Institute of Aeronautics and Astronautics

Table 4 - Yaw oscillation test matrix

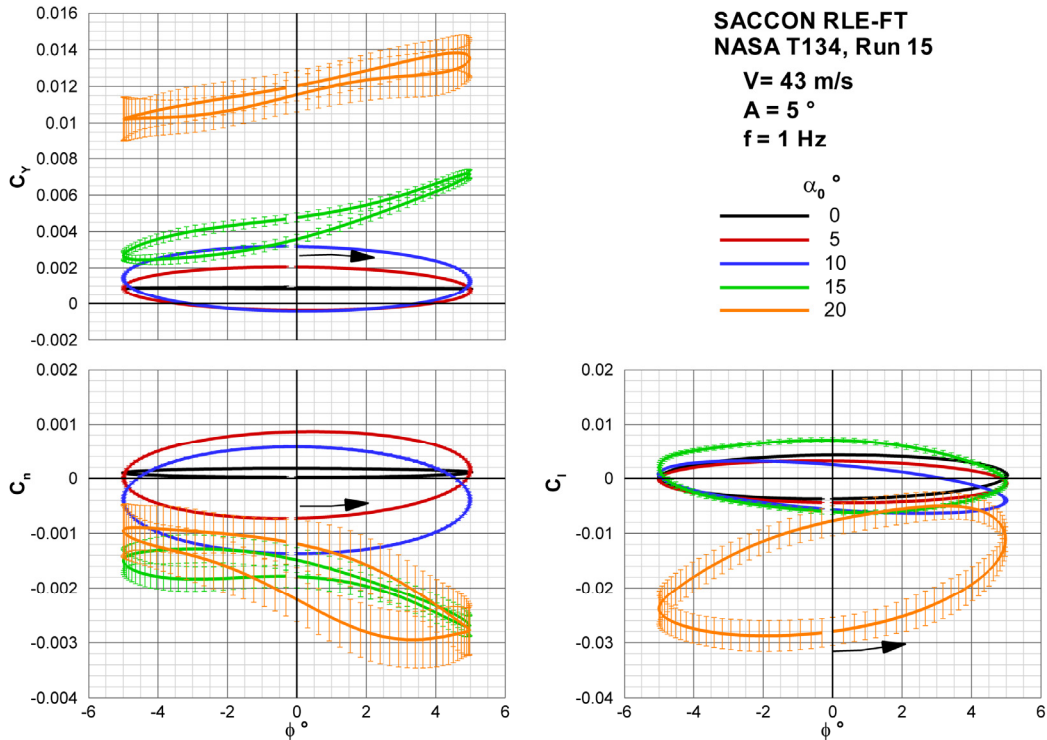| Tunnel	Test	Run	Config.	α deg	Amp deg	f Hz	V m/s	$\frac{\omega b}{2V}$	r_{max} °/s	$\frac{r_{max}b}{2V}$	Duration sec	Mount
DNW-NWB	2373	1033-1042	RLE	0	5	1		0.081	31.4	0.0070	30	0° Yaw link
		1043-1052		0		3		0.242	94.2	0.0211		
		1053-1062		5		1	60	0.081	31.4	0.0070		
		1063-1072		5		3		0.242	94.2	0.0211		
		1073-1082				1		0.081	31.4	0.0070		
		1083-1092				3		0.242	94.2	0.0211		
		1424-1433	RLE-FT	10		1		0.097	31.4	0.0084		15° Yaw link
		1434-1443		10		2		0.193	62.8	0.0169		
		1444-1453		10		3		0.290	94.2	0.0253		
		1454-1463		14		1		0.097	31.4	0.0084		
		1464-1473		14		2		0.193	62.8	0.0169		
		1474-1483		14		3		0.290	94.2	0.0253		
		1484-1493		15		2	50	0.193	62.8	0.0169		
		1494-1503		15		3		0.290	94.2	0.0253		
		1504-1513		20		2		0.193	62.8	0.0169		
		1514-1523		20		3		0.290	94.2	0.0253		
		1524-1533		25		2		0.193	62.8	0.0169		
		1534-1543		25		3		0.290	94.2	0.0253		
NASA 14x22	134	5		5 10		1		0.097	31.4	0.0084	43	Bottom sting
		7		10 14 15								
DNW-NWB	2373	1119-1128	SLE	10				0.081	31.4	0.0070	30	0° Yaw link
		1129-1138		10		2	60	0.161	62.8	0.0141		
		1139-1148		10		3		0.242	94.2	0.0211		
		1335-1344				1		0.097	31.4	0.0084		15° Yaw link
		1345-1354				2	50	0.193	62.8	0.0169		
		1355-1364				3		0.290	94.2	0.0253		
		1305-1314		15		1		0.097	31.4	0.0084		
		1315-1324		15		2		0.193	62.8	0.0169		
		1325-1334		15		3		0.290	94.2	0.0253		
		1285-1294				1	60	0.081	31.4	0.0070		
		1295-1304				2		0.161	62.8	0.0141		
		1365-1374		20		1		0.097	31.4	0.0084		
		1375-1384		20		3	50	0.290	94.2	0.0253		
		1385-1394		25		1		0.097	31.4	0.0084		
		1395-1404		25		3		0.290	94.2	0.0253		
NASA 14x22	134	59			10	1	18	0.264	31.4	0.0231	43	Bottom sting
		62			15				62.8	0.0461		
		65		5 10 15 20 25					94.2	0.0692		
		60			5			0.112	31.4	0.0098		
		63			10		43		62.8	0.0196		
		68		0 5 10 15 20	15	0.05		0.006	4.7	0.0015	100	
		66		5 10 15 20 25	15			0.112	94.2	0.0294		
		61			5	1	50	0.097	31.4	0.0084	43	
		64		5 10 15	10				62.8	0.0169		
		67			15				94.2	0.0253		

American Institute of Aeronautics and Astronautics

Figure 18. Example of AoA effect on roll oscillation 1-cycle averaged lateral-directional force and moment coefficients for RLE-FT configuration.
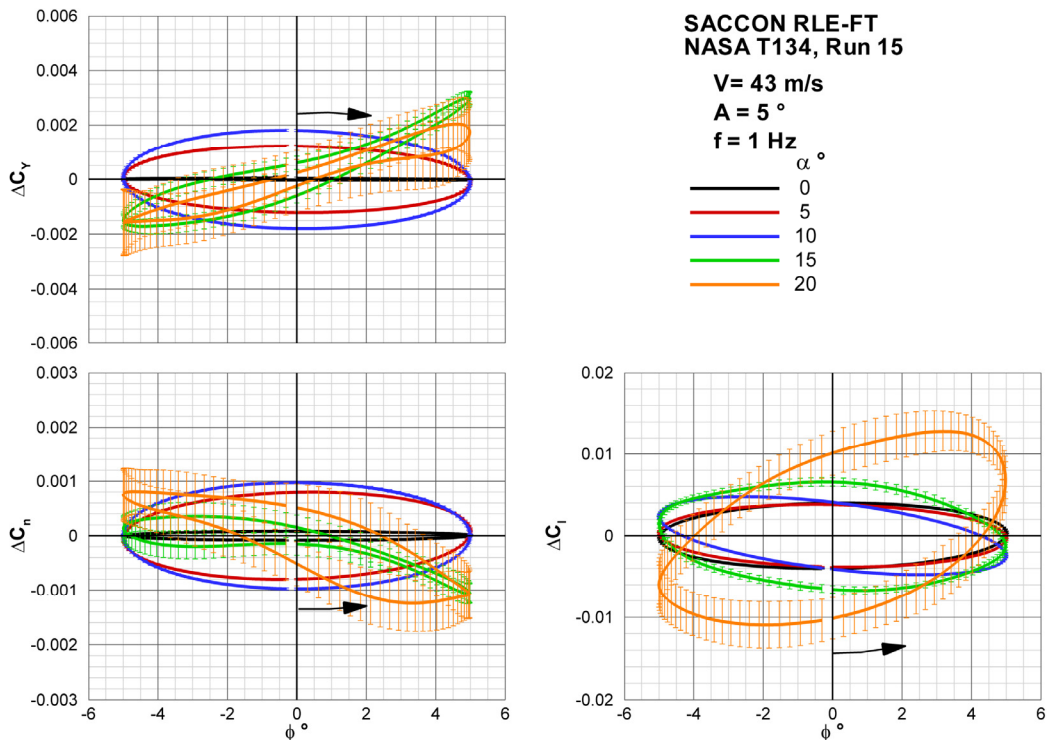

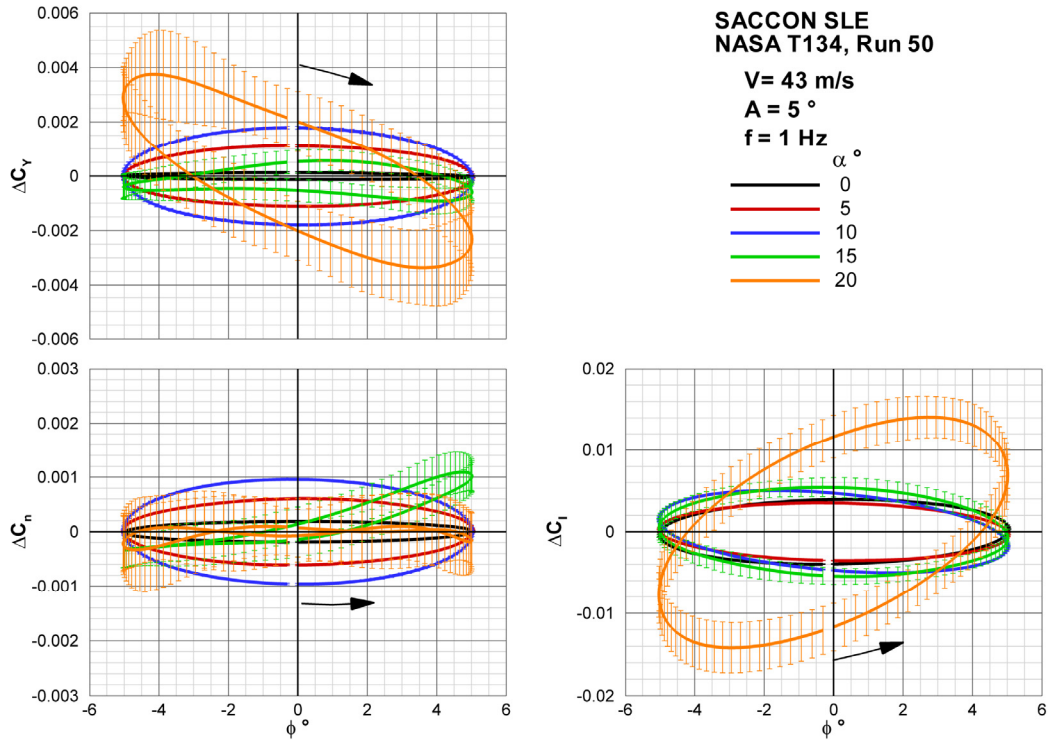**Figure 19. Example of roll oscillation lateral-directional coefficient loops with static offset removed.**

American Institute of Aeronautics and Astronautics

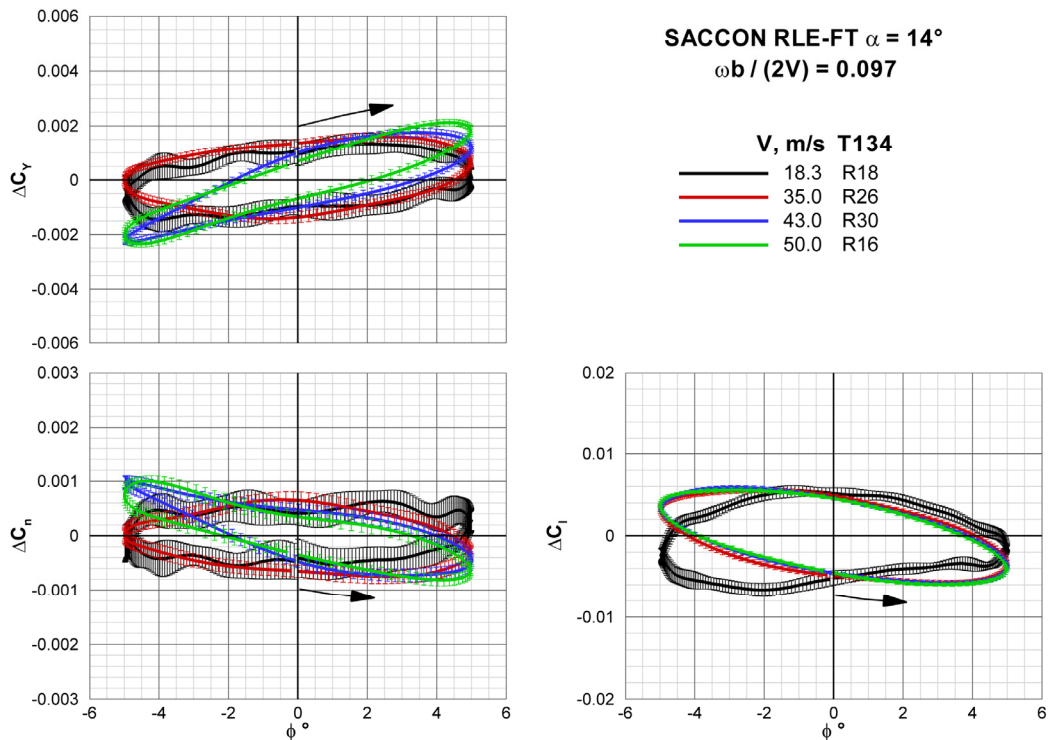**Figure 20. AoA effect on roll oscillation lateral-directional force and moment coefficients for SLE configuration.**

Figure 21. Roll oscillation velocity effect at a constant reduced frequency and amplitude for RLE-FT about 14° nominal AoA.

American Institute of Aeronautics and Astronautics
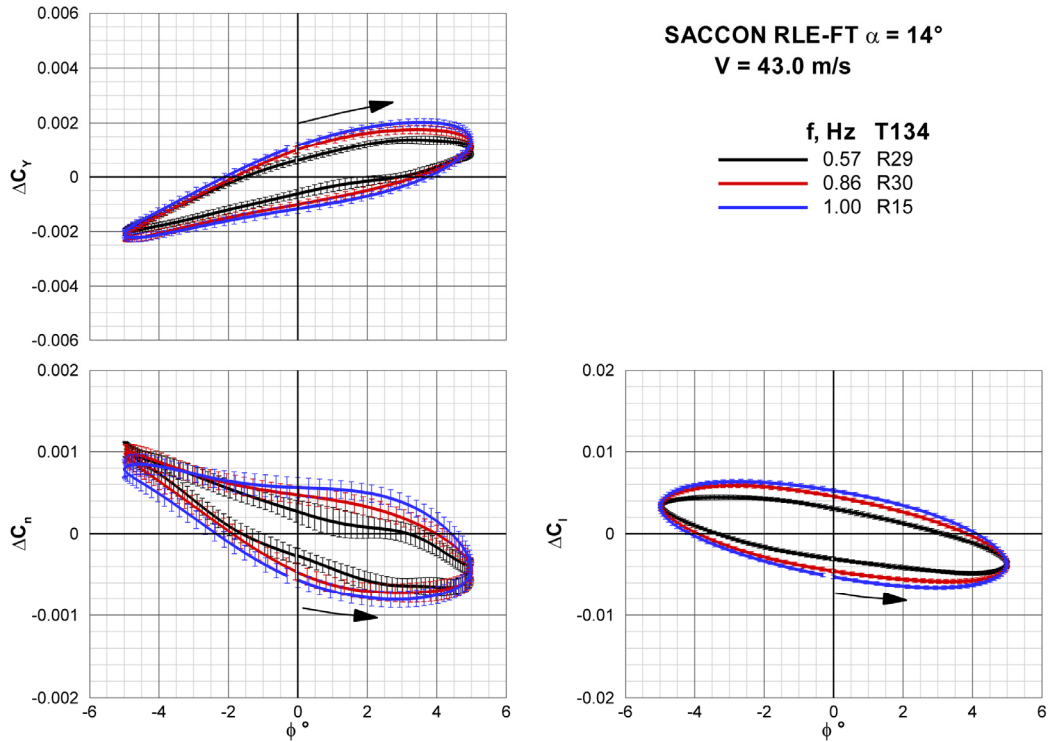
Figure 22. Roll oscillation frequency effect for RLE-FT about 14° nominal AoA.
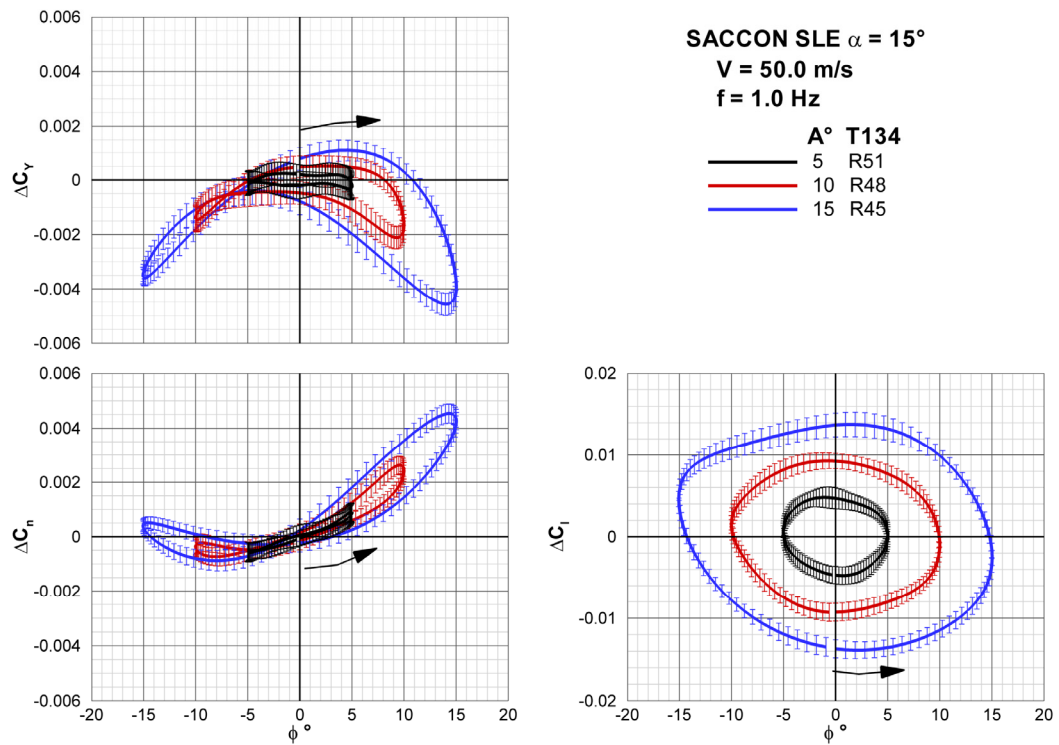
Figure 23. SACCON SLE roll oscillation amplitude effect about 15° nominal AoA.
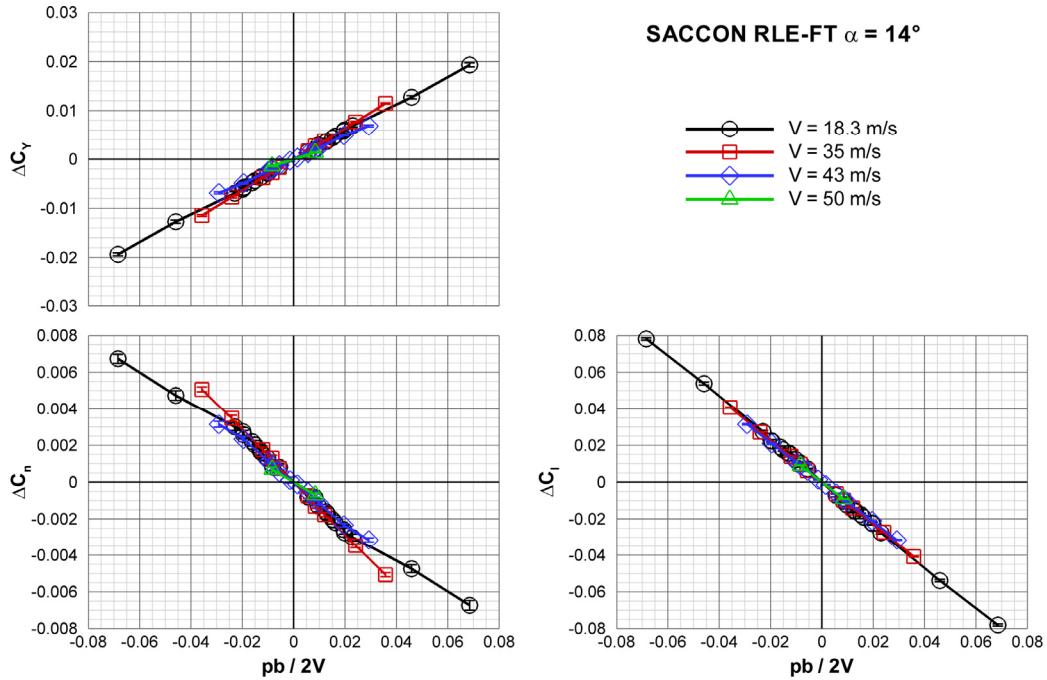
Figure 24. Peak roll rate coefficient values for RLE-FT configuration at 14° nominal AoA.
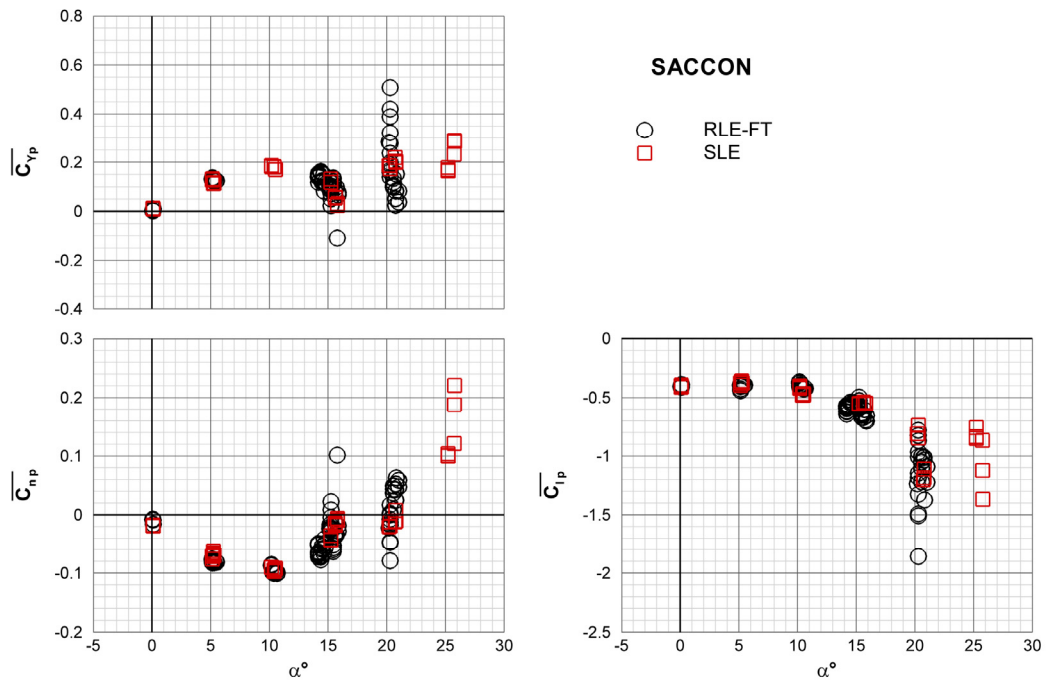
Figure 25. Roll axis combined dynamic derivatives.
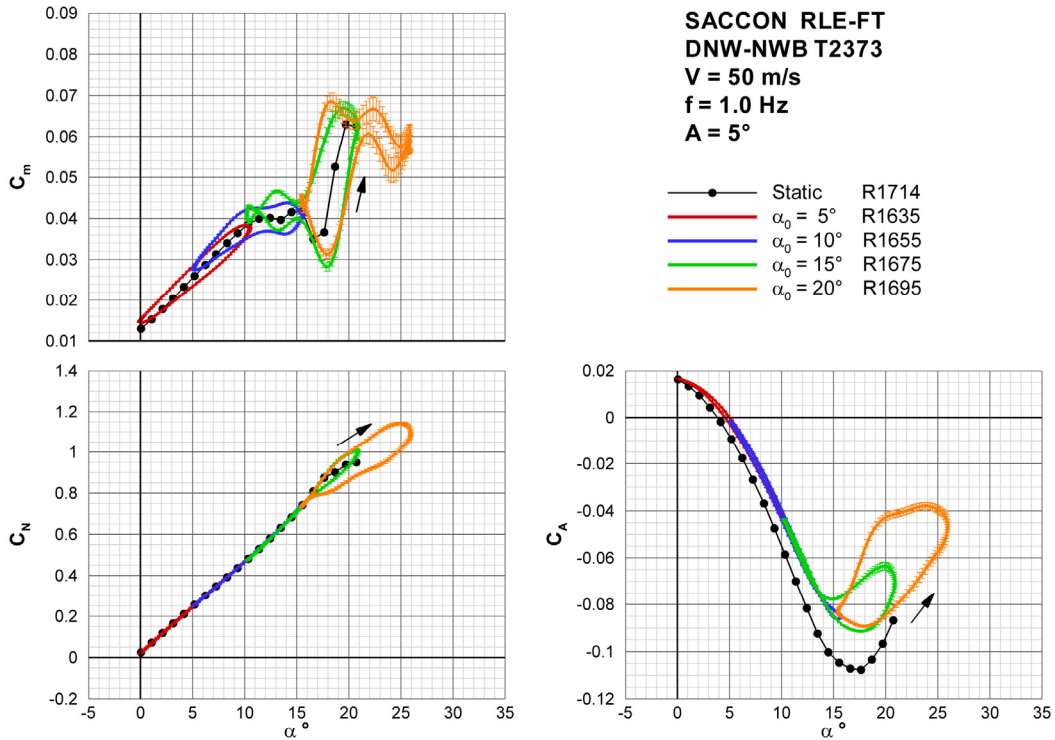
Figure 26. RLE-FT static and dynamic pitch oscillation longitudinal force and moment coefficients about 5°, 10°, 15° and 20° nominal AoA at 1 Hz.
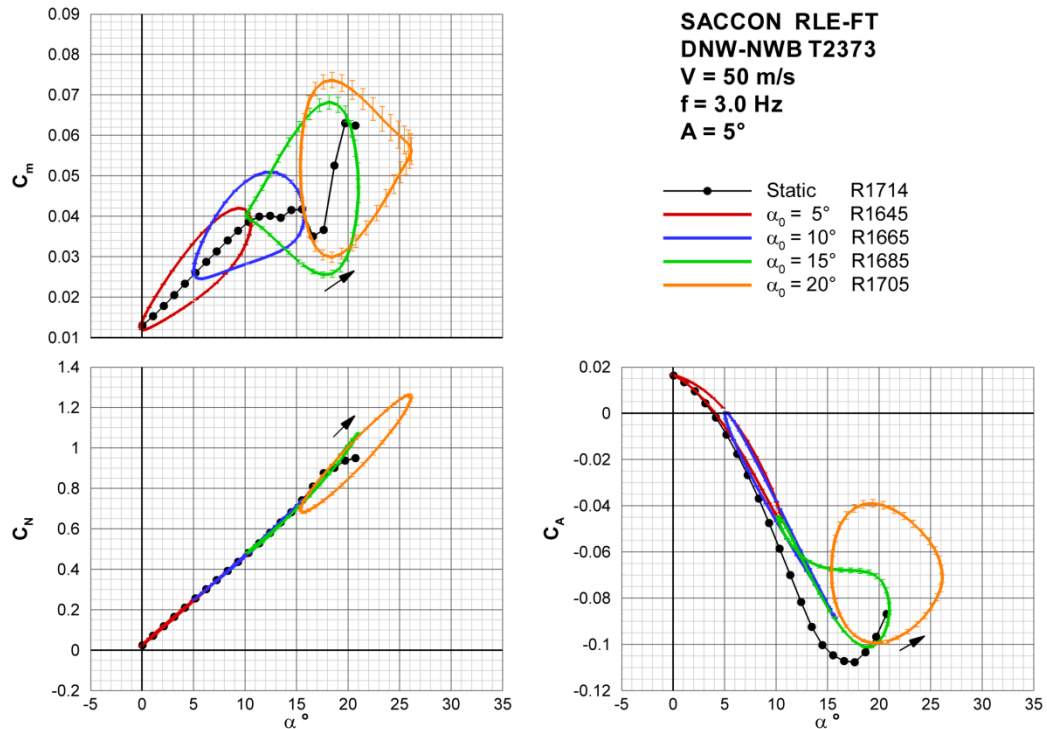
Figure 27. RLE-FT static and dynamic pitch oscillation longitudinal force and moment coefficients about 5°, 10°, 15° and 20° nominal AoA at 3 Hz.

American Institute of Aeronautics and Astronautics
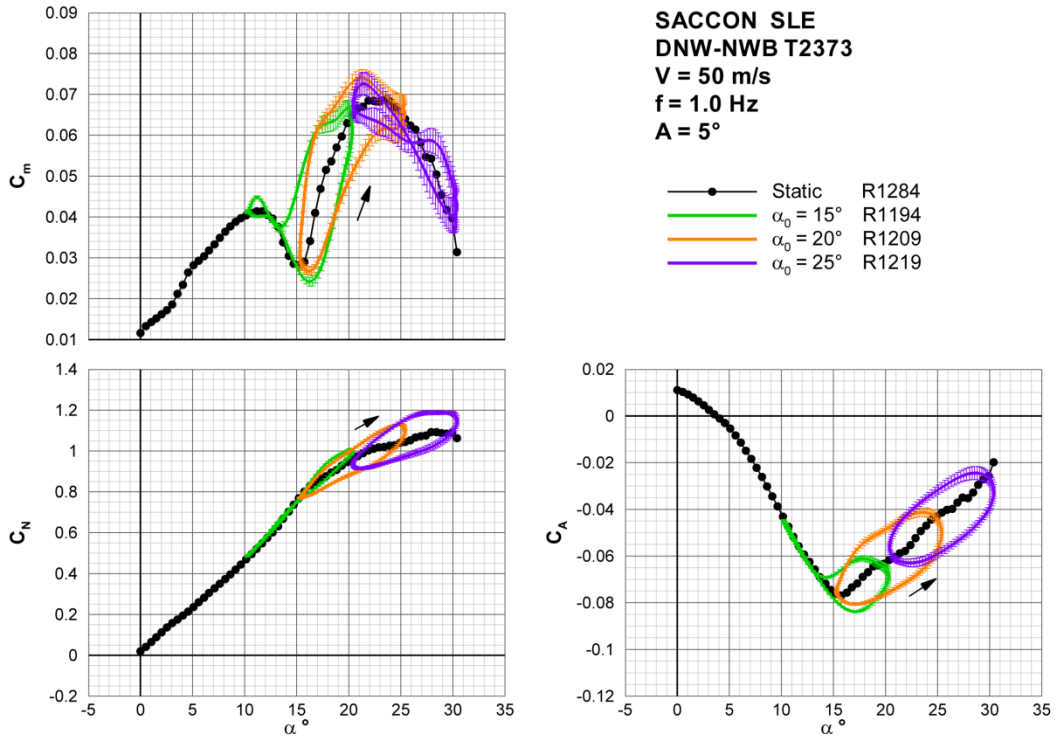
Figure 28. SLE static and dynamic pitch oscillation longitudinal force and moment coefficients about 15°, 20° and 25° nominal AoA at 1 Hz.
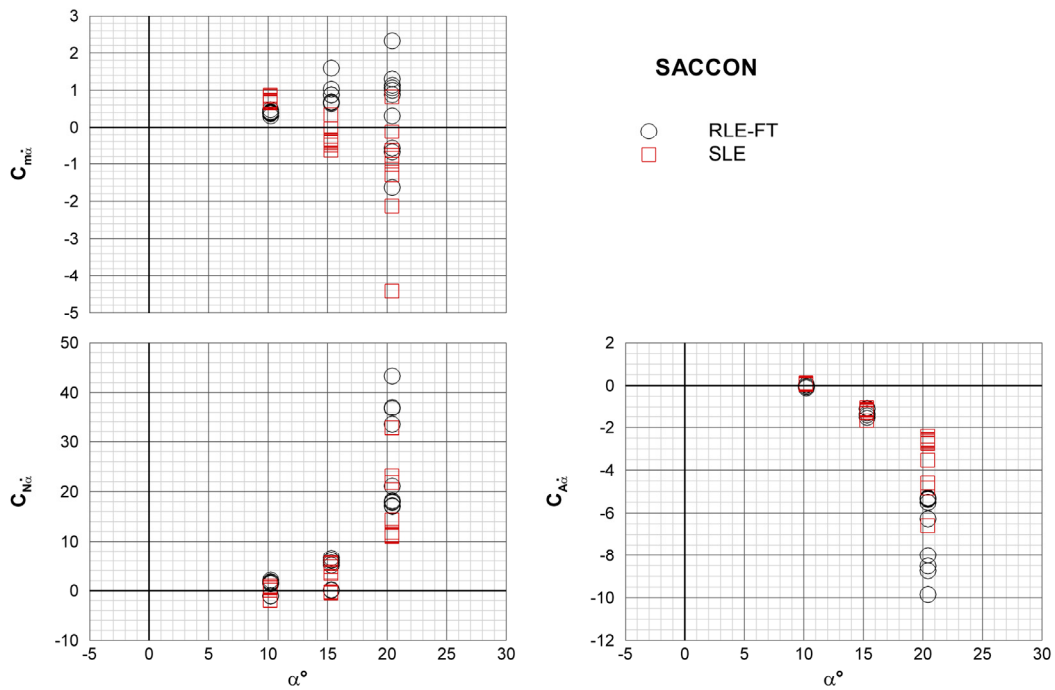
Figure 29. Pitch axis combined dynamic derivatives.

American Institute of Aeronautics and Astronautics
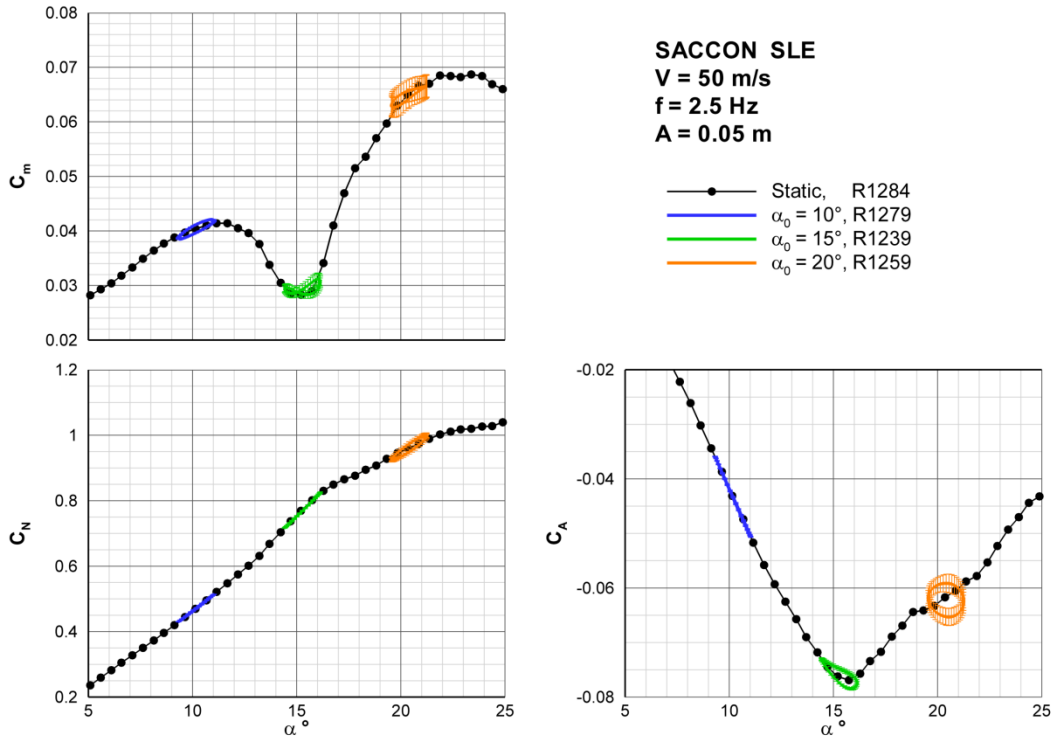
Figure 30. SLE static and dynamic longitudinal force and moment coefficients for plunging about 10°, 15° and 20° nominal AoA at 2.5 Hz.
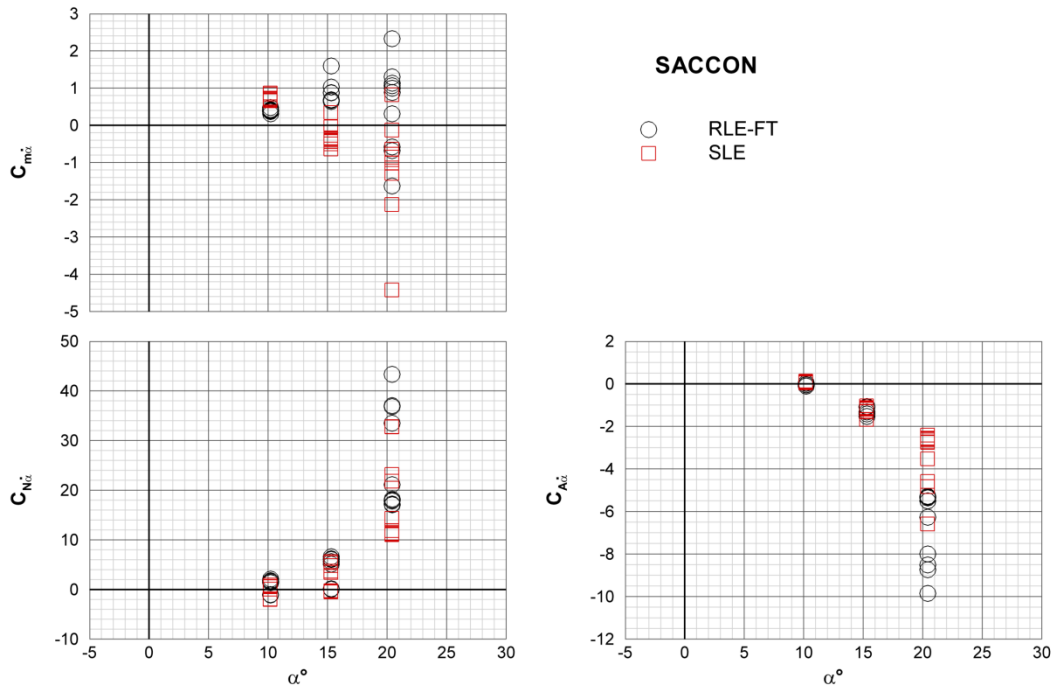
Figure 31. Longitudinal angle of attack rate derivatives.
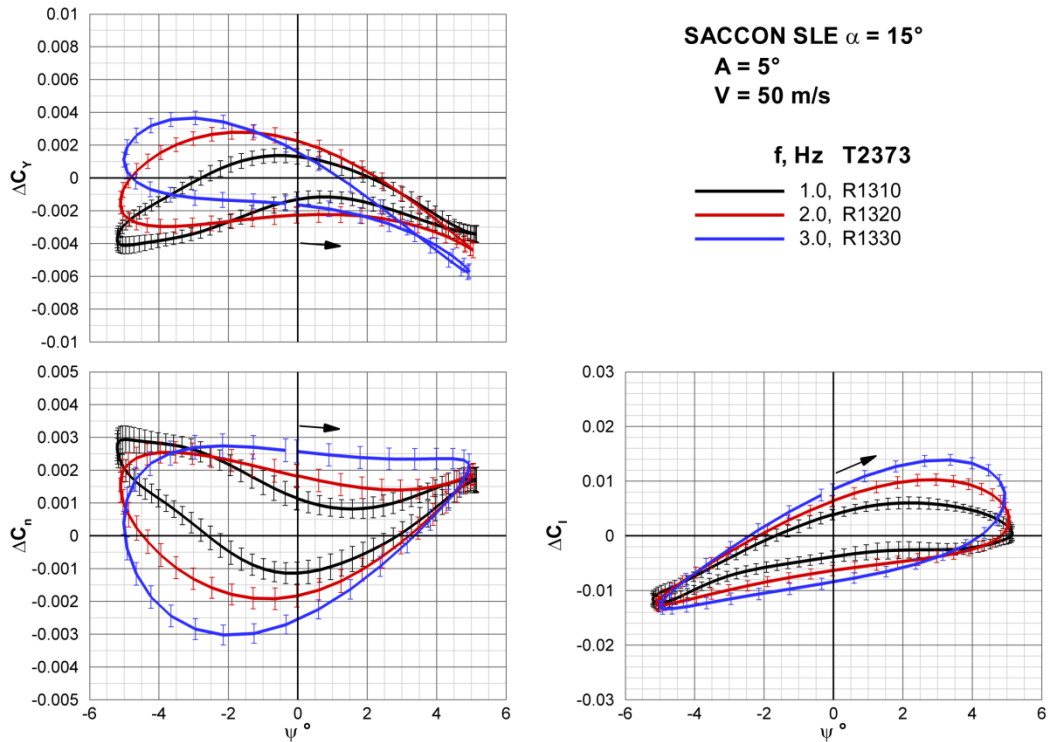
Figure 32. Yaw oscillation frequency effect at a constant velocity and amplitude for SLE about 15° nominal AoA.
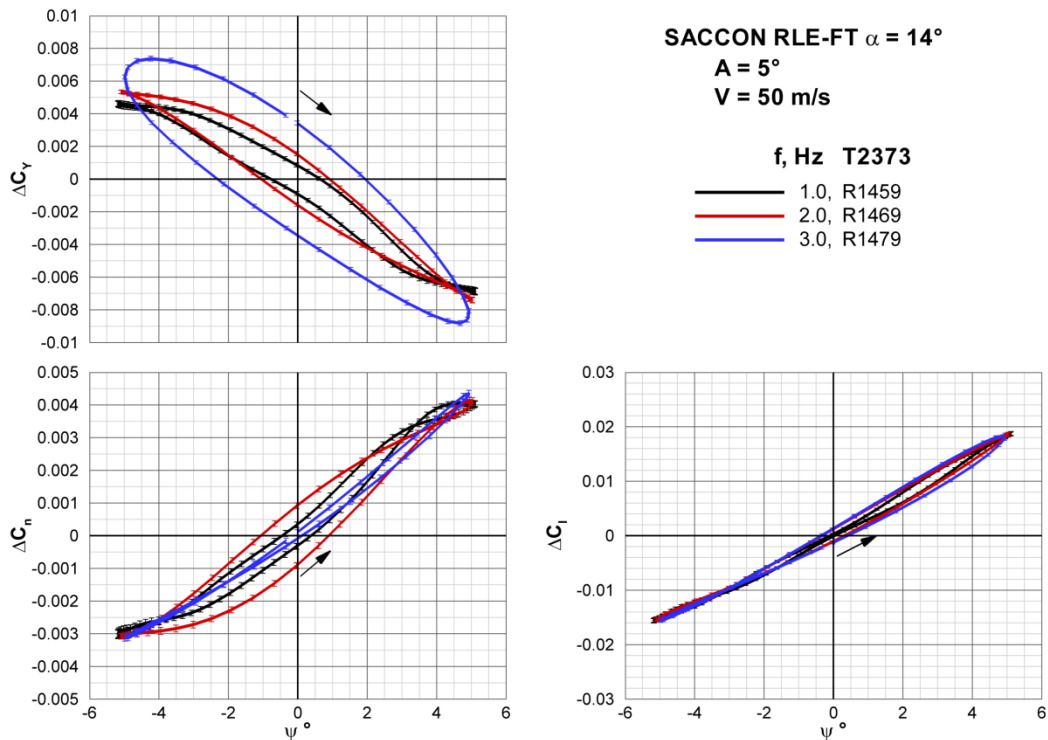
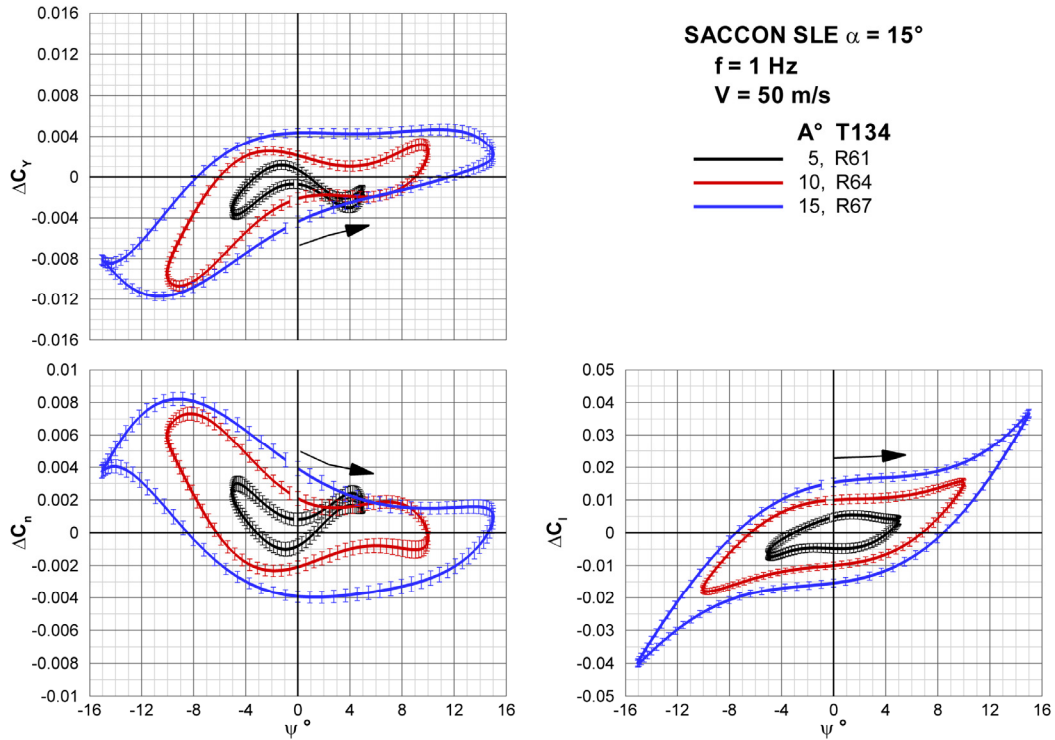**Figure 33. Yaw oscillation frequency effect at a constant velocity and amplitude for RLE-FT about 14° nominal AoA.**

American Institute of Aeronautics and Astronautics

Figure 34. Yaw oscillation amplitude effect at a constant frequency and velocity for SLE about 15° AoA.
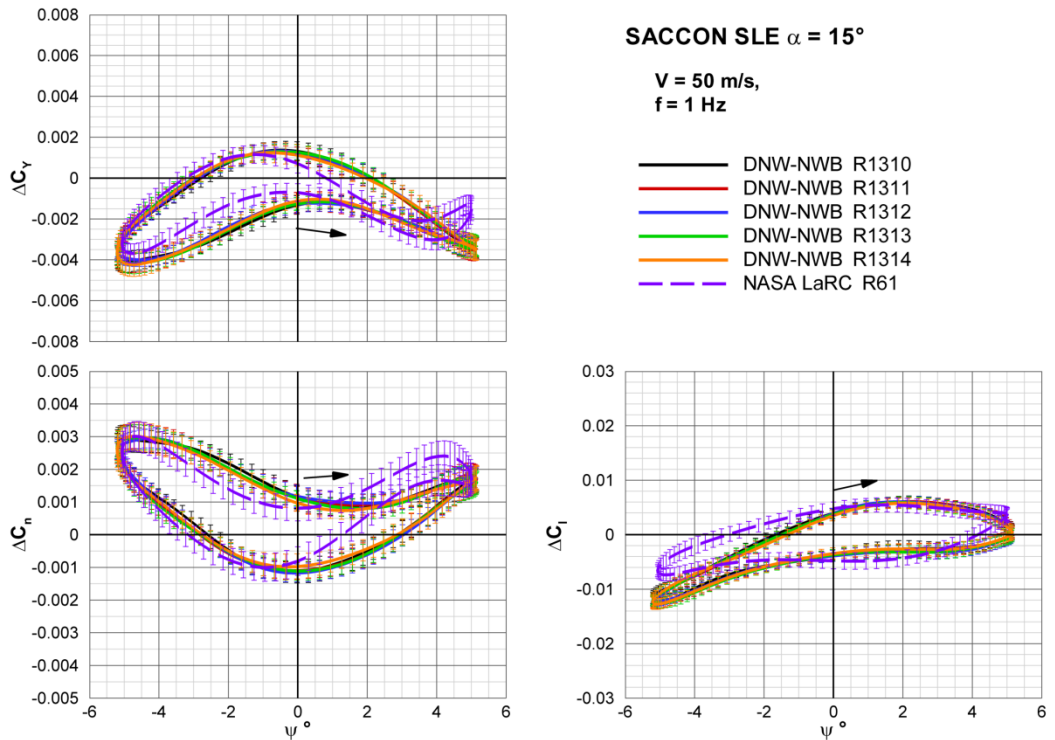
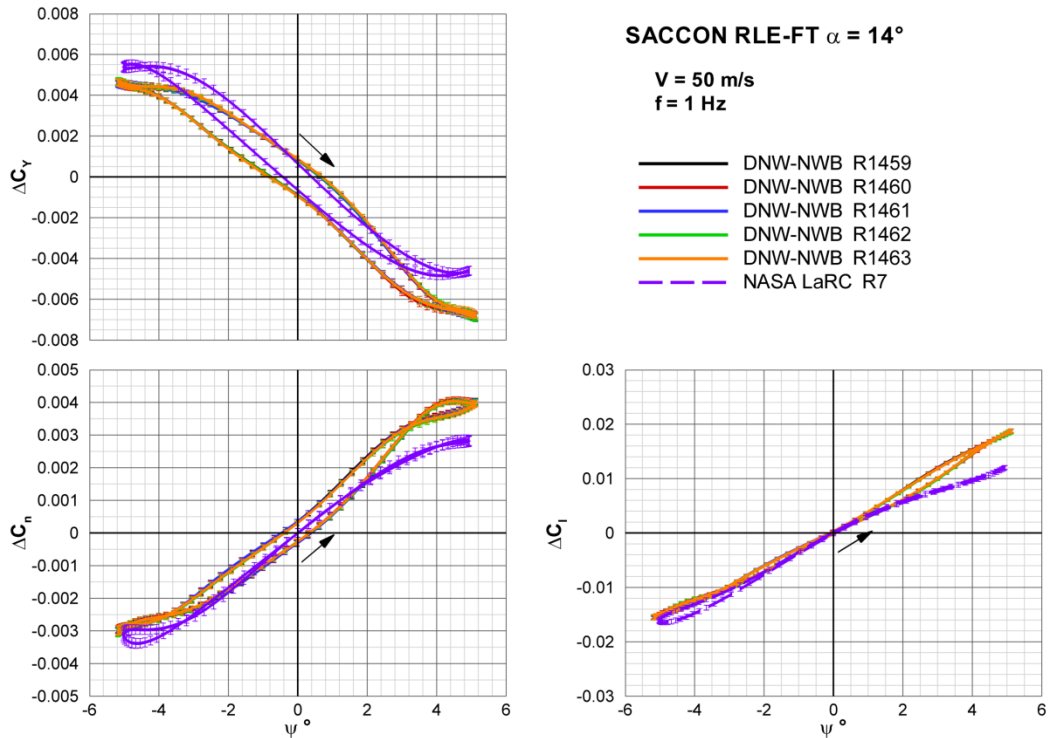**Figure 35. SACCON SLE yaw oscillation DNW to NASA test comparison about 15° nominal AoA.**

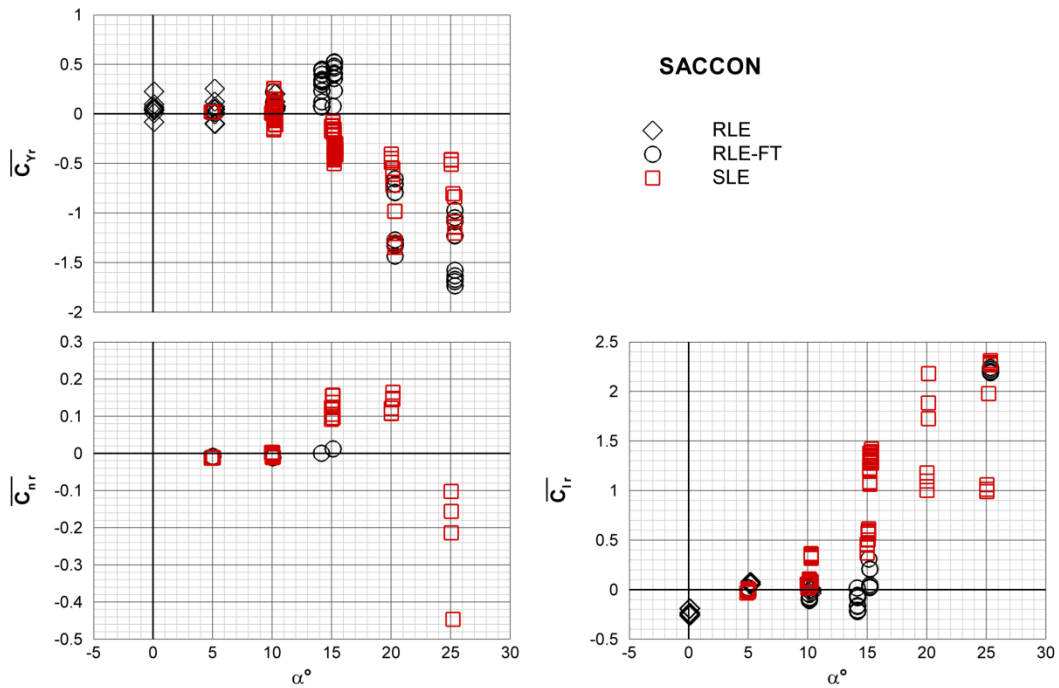**Figure 36. SACCON RLE-FT yaw oscillation DNW to NASA test comparison about 14° nominal AoA.**

Figure 37. Yaw axis combined dynamic derivatives.

American Institute of Aeronautics and Astronautics